Experimental Thermal and Fluid Science 145 (2023) 110888

Contents lists available at ScienceDirect

Experimental Thermal and Fluid Science

journal homepage: www.elsevier.com/locate/etfs

A comparative study of circular and rectangular bended plunging jets

Giorgio Moscato [a,*], Giovanni Paolo Romano [a]

[a] University of Rome "Sapienza", via Eudossiana 18, Rome 00184, Italy

ARTICLE INFO

Keywords:
Plunging jet
Mixing
Entrainment
Asymmetrical jets
PIV

ABSTRACT

In the present work we study the topology, mixing properties, turbulence quantities, dependence on the outlet geometry of a sharp-edged orifice plunging jet which first issues horizontally in air and then plunges in a water pool. The investigated orifices shapes are circular and rectangular. Data are acquired at different Reynolds numbers in the range 11000–25000, based on the orifice diameter (equal to 2 cm) and on the average exit velocity, as derived from flow rate measurements. Velocity fields in vertical and horizontal planes are measured using planar time-resolved Particle Image Velocimetry. Results show a clear asymmetry of the cross-velocity profiles both in circular and rectangular cases, with the latter that revealed a shape which is Reynolds number dependent. Axial velocity decays, potential core lengths and spreading rates highlight an opposite trend between the two jet geometries, thus suggesting a higher mixing for the lowest Reynolds number circular jet and the highest rectangular one. Plunging angle shows a dependency on Reynolds number. Moreover, it seems to play a role in the evolution of the upper and lower side of the jet due to the onset of a co-flow. Ambient mass entrainment points out the different interactions of the two plunging jets with the ambient flow: in circular case, it entrains fluid from the surroundings, from horizontal to vertical planes in streamwise direction, while in rectangular one it ejects flow from vertical to horizontal planes. Finally, Strouhal numbers are derived for main vortices frequencies along jet centerline, other than upper and lower sides.

1. Introduction

Water plunging jets are encountered in many industrial and civil applications like chemicals stirrers [12], steel industry, food industry [3], water sewage systems, as well as in natural processes like waterfalls and rivers self-purification. One of the main features of plunging jets is their mixing ability in comparison to free jets. This is connected to a greater ambient fluid entrainment due to a greater turbulent production, an early onset of primary vortices and thus a higher exchange of momentum [4]. This feature plays a key role in every application where a fast and diffuse turbulent mixing is required. However, those jets are characterised also by an air entrainment process so that air bubbles are captured below the free surface thanks to a sufficiently high jet velocity (say, the critical velocity) and to the extent of disturbances moving with the jet [5]. For this reason, plunging jets are important in application for which a cheap and effective oxygenation of liquids is required [6]. Though, air entrapment can also lead to negative effects such as choking of sewer ducts and manhole due to the free cross section area reduction for the flow rate discharge. Thus, the study of this class of jet flows is relevant from both application and fundamental research points of view.

Hassan and colleagues [4] studied a free falling vertical plunging jet issuing from a circular nozzle for five Reynolds numbers (from 3000 to 10000) with time-resolved particle image velocimetry (PIV). They found that primary vortical structures form right below the plunging point, presumably due to the interaction with the free surface, thus leading to an early entrainment. The early formation of vortices, in comparison to free jets, results in an early breakdown so that a premature merge of the shear layers and potential core end take place. Ambient entrainment was considered by means of the mass entrainment ratio (i.e. differences between the mass flow $\dot{m}$ evaluated at two consecutive jet cross-sections) and the entrainment coefficient $C_E = \frac{D}{\dot{m}_0}\left(\frac{d\dot{m}}{dx}\right)$ (where D is the nozzle diameter and $\dot{m}_0$ is the initial mass flow rate). They observed a reduction of these values by increasing the Reynolds number. Furthermore, Hammad [7] investigated a fully developed circular turbulent jet issuing from a vertical pipe and impacting on a water pool, using PIV. He performed the measurements for two Reynolds numbers (namely, 13000 and 23000) and four nozzle-to-interface separation distances H (i.e., H/D=-1, 0, 1, 2, where H/D < 0 means a submerged nozzle condition). He found that at Reynolds number equal to 13000, no air bubble is entrapped into the main jet. At Reynolds number equal to 23000 and H/D=1, only individual bubbles are entrained, while for H/D>1 an air

* Corresponding author.
E-mail address: giorgio.moscato@uniroma1.it (G. Moscato).

https://doi.org/10.1016/j.expthermflusci.2023.110888
Received 22 November 2022; Received in revised form 3 February 2023; Accepted 28 February 2023
Available online 9 March 2023

Nomenclature

A_{pp}	jet cross section area at the plunging point [m^2]
D	orifice diameter [m]
d_{pp}	jet diameter at the plunging point [m]
g	gravity acceleration [m/s^2]
h	distance between the pool free surface and the orifice's center [m]
K_u	axial velocity decay factor
l	*iso*-velocity line abscissa [m]
Q	total volumetric flow rate [m^3/s]
Q_{low}	volumetric flow rate derived in the lower part of the jet [m^3/s]
Q_r	volumetric flow rate in horizontal planes [m^3/s]
Q_{up}	volumetric flow rate derived in the upper part of the jet [m^3/s]
ρ_{uu}	Cross-correlation function (dimensionless)
r	equivalent radius derived from each *iso*-velocity line total length $\left(\frac{l_{tot}}{2\pi}\right)$ [m]
T	water temperature within the pool [°C]
t_{fall}	falling time of the jet [s]
t_0	initial falling time [s]
U_{cl}	velocity along jet centerline [m/s]
U_r	velocity component normal to *iso*-velocity line abscissa [m/s]
U_0	velocity derived from flow rate measurements [m/s]
U_{pp}	velocity at the plunging point [m/s]
U_{yfall}	vertical component of the velocity at the plunging point due to gravity [m/s]
u_{reproj}	streamwise velocity component [m/s]
u'_{reproj}	streamwise velocity fluctuation [m/s]
v_{reproj}	normal velocity component [m/s]
x	streamwise direction axis [m]
X_1	horizontal axis [m]
y	normal axis to streamwise direction [m]
Y_1	vertical axis [m]
$y_{1/2}$	jet half-velocity width [m]
Z_1	axis normal to X_1Y_1-plane [m]

Greek symbols

θ	inclination angle between jet and horizontal free surface at the plunging point [°]
μ_w	dynamic viscosity of the water [Pa·s]
$\sigma_{x1,2}$	standard deviation of velocity at position x_1 and x_2
τ	lag time in cross-correlation function [s]
τ_p	response time of the seeding [s]
τ_0	characteristic time scale of the flow [s]

cavity is formed, whose extension is proportional to the nozzle-to-interface distance. Nevertheless, Kiger and Duncan [8] in their review underlined air entrapment dependence on intrinsic properties of both gas and liquid phases (such as density and viscosity), along with disturbances extent, plunging angle and non-dimensional parameters like Froude number, Weber number and Capillary number.

Recently, Shrivastava and colleagues [9] studied the possibility to use a confined plunging jet as an outfall of the desalination brine as a variant of the more-classical plunging jet liquid reactor.

In such a scenario, several geometrical, kinematic and dynamic parameters are involved, mainly jet outlet type (pipe or nozzle), shape and the Reynolds number. In addition to Reynolds number, the jet shape plays an important role in ambient mass entrainment. Indeed, it is possible to increase mixing between jet flow and the environment by choosing a non-circular shape for the jet outlet. In particular, rectangular and elliptic jets were reported to have the highest entrainment rate compared to round, triangular, daisy or two-dimensional jets thanks to a phenomenon called "axis switching" (on large-scale) and higher azimuthal instability modes (on small-scale) [10111213]. Axis switching is an apparent 90° rotation of the free jet cross section which is observed for non-symmetric jets and it is ascribed to a different growth rate of the shear layers in the major and minor axis plane owing to the natural roll-up of the vortex rings with a non-uniform azimuthal curvature [1014]. It was observed also for free falling water jets where it is ascribed to the competition of the surface tension, which tries to minimize the jet cross shape, and the lateral-inertial forces [1516].

Mixing properties also depend on upstream boundary conditions. Pipe jets are found to be the least effective due to their low production of coherent structures in the near-field region compared to the contoured nozzle or orifice configurations [17]. These structures in nozzle jets are more easily detected than the ones in the orifice jets, but their frequency is generally lower so that the latter exhibit a higher entrainment rate [18]. This is confirmed by Quinn [19], who studied a round jet from a contoured nozzle and a sharp-edge orifice. He found a lower potential core length, a higher mean centreline decay, a higher jet half-velocity width decay, a smaller turbulence intensity peak distance along the jet centreline and higher streamwise Reynolds normal stresses in comparison to the nozzle jet.

With respect to Reynolds number effect, several Authors focused on its role in jets turbulent and mixing features. For a planar air jet, at moderate Reynolds numbers (1000–7000), a constant dominant vortex passage frequency at the end of the potential core (in the near field) and constant integral scale measurements in the far field were found for all the considered velocities, so that the large-scale eddies seem not to be influenced by the Reynolds number [20]. At the same time, by increasing Reynolds number (but still in the moderate interval), large scale structures' energy decreases thus resulting in a weaker mixing. Same results were obtained also by Suresh and colleagues [21] who investigated a plane turbulent air jet for Reynolds number between 250 and 6250. It was characterized by large scale vortices and high flow intermittency, thus showing larger ambient entrainment and higher jet decay than high Reynolds number jets, with the latter characterized by finer scale structures observed even in the near field.

For higher Reynolds numbers, mean centreline velocity and half-velocity width reveal a significant dependence up to $Re \approx 10^4$, from which they remain almost constant till about $Re = 2 \times 10^4$ [2223]. In their work, Hashiehbaf and Romano [24] analysed the impact on the jet turbulent features of different orifices shapes in a range of Reynolds number between 8000 and 35000. They concluded that the axial and radial distributions of turbulence intensity, along with Reynolds shear stresses, suggest the separation of the jets behaviours into two groups based on their similarity: square-triangular and elliptic-rectangular orifices. Again, the best mixing properties belong to the rectangular and elliptic shapes in the near field, while switching to the square one in the far field.

Despite the large amount of works about free jets characteristics and motion, literature on plunging jets is still somewhat limited to specific aspects. Indeed, most of the works connected to them are mainly focused on the analysis and quantification of air bubbles entrainment [5,25,261,3,27–3132]. To the best authors' knowledge, there are only few works which deal with the study of the plunging jet motion field [334,34735] and they refer mostly to a vertical plunging jet configuration or air bubbles entrapment. However, there are plenty of application for which the jet impacts with the receiving water pool with different inclination angles [36,37]. Moreover, there is lack of comprehension on how factors as outlet shape contribute to the

turbulent mixing properties of a plunging jet.

To sum up, the aim of this work is to study a sharp-edged orifice's plunging jet which first issues horizontally in air and then plunges in a water pool with limited generation of air bubbles. Different orifice shapes, namely circular and rectangular, are tested via high-speed Particle Image Velocimetry so that time-resolved information are extracted. In order to focus the analysis on relevant flow features, we test specific boundary conditions where almost no air entrainment occurs, *i.e.* the jet impact velocity is lower or very close to its critical air entrainment value [5]. The results provide shedding light onto the turbulent features of such a flow field and prove to be useful for applications design and validation of numerical simulations.

2. Experimental set-up

In order to study the plunging jets behaviour, a closed-loop flow system was implemented. It is composed of a main test plexiglass tank, a valve system to measure the volumetric flow rate, a wide discharge tank where a centrifugal pump pushes the water flow up to an open overflow reservoir raised 2 m above the ground, from which the flow fells to the plexiglass tank due to gravity. The latter is divided into two parts by a sharp-edged orifice plate: the first one is a pressurized settling chamber while the second one is the open-air water plunging pool. In order to keep the level of the free surface constant, we implemented an overflow draining system which fixes the height value of about 11.5 cm from the pool floor.

Flow rate is controlled by a ball valve after which a honeycomb smooths the large-scale vortical structures before the flow enters in the plexiglass tank. A schematic sketch of the system is reported in Fig. 1 for better clarity. The selected sharp-edged orifice shapes are circular and rectangular. This choice let us investigate and compare a symmetric and a clearly non-symmetric condition, with the latter that represents the best solution in term of mixing properties for free jets [10111213]. The orifice area is the same for both plates (equal to 100π mm^2), so that an equivalent diameter D of length 0.02 m is defined and used to evaluate the Reynolds number. Rectangular orifice edges have a length of 10.23 mm and 30.70 mm, so that the aspect ratio (i.e. longest edge divided by shortest edge) is about 3 (Fig. 2). Both orifices are cut with a 45° angle and have been already investigated for free jets in Hashiehbaf and colleagues works [2438]. The distance between orifices' central point and the free surface is about 7 cm (≈3.5D). Volumetric flow rate, thus the velocity U_0, is measured at the outlet of the plexiglass tank through a graduated volume. By recording its filling time with a chronometer (whose precision is in the order of a hundredth of a second), volumetric flow rate is computed as the ratio of the filled volume over its filling time. The typical time length of each measurement is about 1 min. In order to reduce measurement uncertainties due to water flow oscillations, graduated volume scale and time recordings, a sufficiently large volume (about 17 L) is filled at least three times for every Reynolds number condition. The maximum standard deviation value of the flow rate measurements is about 1%, but it is often well below 0.5%. Water temperature in the water pool is also recorded with a thermometer with a precision of ± 0.1 °C and considered for kinematic viscosity.

In Table 1 we report a list of all the investigated conditions both for circular and rectangular jets, along with their Reynolds number (Re_D), Weber number (We), Capillary number (Ca) and Froude number (Fr), defined as:

$$Re_D = \frac{U_0 D}{\nu};\ We = \frac{\rho U_0^2 D}{\sigma};\ Ca = \frac{We}{Re} = \frac{\mu_w U_0}{\sigma};\ Fr = \frac{U_0^2}{gD}$$

where the characteristic length scale is taken as the equivalent diameter of the orifice D, U_0 is the velocity from the flow rate measurements, ν and μ_w are respectively the kinematic and dynamic viscosity of water, σ is the surface tension of water-air and g is the gravity acceleration.

A planar time-resolved PIV technique was used to study a vertical plane passing through the jet axis and two horizontal planes at the height of 4.5 cm and 7 cm above the pool floor (thus at $Y_1/D \approx 2.25$ and $Y_1/D \approx 3.5$ respectively) (green planes in Fig. 1).

The flow was seeded with spherical glass particles of mean diameter equal to 15 μm and standard deviation 10 μm (response time [39] $\tau_p = \frac{\rho_p d_p^2}{18\mu_f} \sim 10^{-5}$ *s*, Stokes number $Stk = \tau_p/\tau_0 \sim 10^{-3}$, where subscription "p" refers to particle, "f" to fluid and τ_0 is the characteristic flow time scale).

Images were collected with a high-speed camera FastCam Mini AX100 by Photron (12-bit monochrome, full resolution recordings of about 1 Mpx up to 4000 fps), with a resolution of 1024 × 1024 pixels, a frame rate of 2000 fps for all the considered flow velocities and a total amount of 5454 pictures for every experimental configuration. A nine partitions recording scheme was used in order to improve the quality of the statistical results owing to the statistical independency of the partitions [40]. Each of these subsets took about 0.303 s, to be compared to the integral time scales $\frac{D}{U_{min}} \approx 0.037s$ and $\frac{D}{U_{max}} \approx 0.0168s$ for the lowest

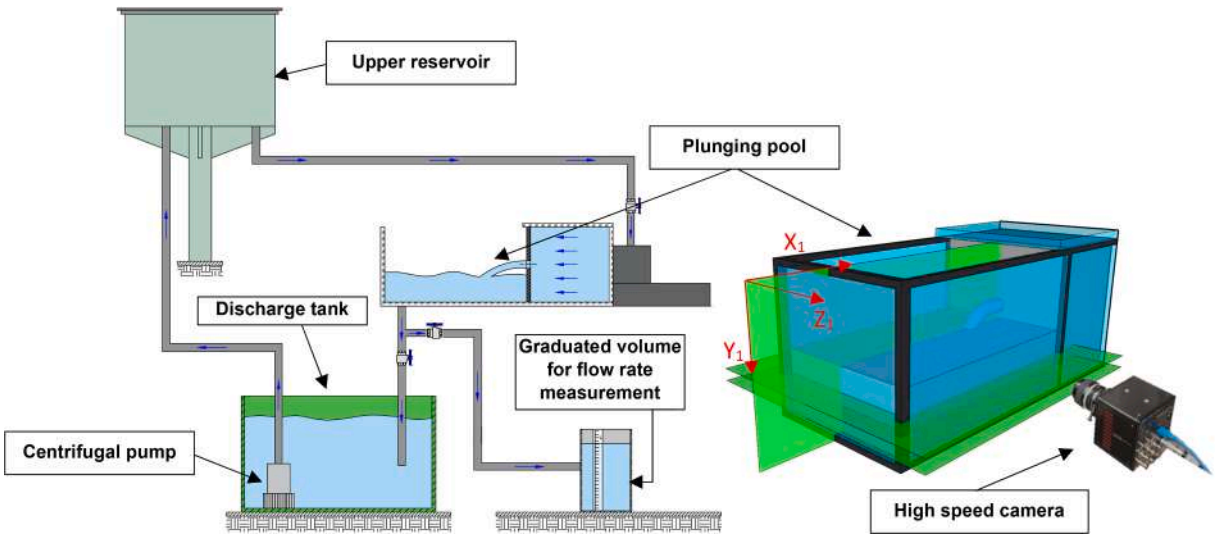

Fig. 1. Sketch of the entire experimental apparatus (flow direction is indicated by blue arrows). Three planes are investigated through PIV technique (green planes in the pictures on the right): one (vertical) passing through the jet's axis and two (horizontal) respectively at about 4.5 cm ($Y_1/D \approx 2.25$) and 7 cm ($Y_1/D \approx 3.5$) from the pool's floor. Reference frame (X_1, Y_1, Z_1) is reported in red. (For interpretation of the references to colour in this figure legend, the reader is referred to the web version of this article.)

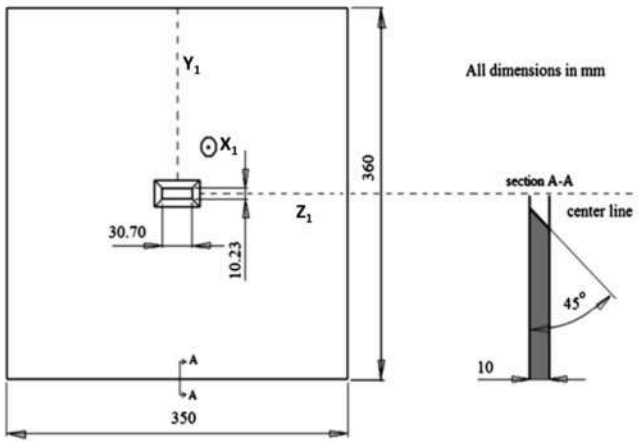

Orifice	Major axis [mm]	Minor axis [mm]	Area [mm²]
circular	20	20	100π
rectangular	30.7	10.2	100π

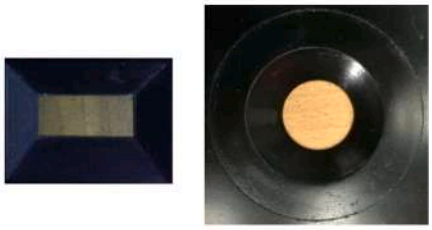

Fig. 2. Details of the rectangular orifice with sharp edge (on the left), orifices dimensions (top-right) and real pictures of rectangular and circular orifices (on the right bottom side).

Table 1
Investigated conditions both for circular and rectangular jets; temperature and velocity (as derived from the flow rate measurement) are reported along with the following non-dimensional groups: Reynolds number, Capillary number, Weber number and Froude number.

Orifice	T [°C]	U_0 [m/s]	Re_D	Ca	We	Fr
Circular	22	0.53	11,000	0.0069	77.58	1.2
Circular	23	0.83	18,000	0.0108	194.48	1.9
Circular	23	1.19	25,500	0.0154	394.15	2.7
Rectangular	24	0.59	13,000	0.0074	96.41	1.3
Rectangular	24	0.66	15,000	0.0083	121.38	1.5
Rectangular	23	0.88	19,000	0.0114	216.63	2
Rectangular	24	1.13	25,000	0.0143	357.18	2.6

(U_{min}) and highest (U_{max}) considered velocities, respectively. So far, each partition corresponded to about 8 time scales in the former case and 18 time scales in the latter. A time interval of about 30–60 *s* was waited between two consecutive partitions recordings. The camera was placed on the side of the plunging pool for vertical plane investigations (as in Fig. 1), while it was put on the top when measuring on horizontal planes. The laser planes were produced with a 5 W CNI MGL-N-532 continuous diode laser of wavelength 532 ± 1 nm with a thickness of about 3 mm. Images pre-processing, PIV analysis and data post-processing were performed in MATLAB through the software PIVlab [41] and self-created scripts.

At pre-processing stage, the minimum image is computed and subtracted for each recorded set in order to remove background. Contrast-limited adaptive histogram equalization (CLAHE) was also applied aiming to improve the probability of detecting particles [41]. A 630 × 1023 pixels region was chosen (which corresponds to about 12 × 20 cm^2, thus ~ 6D × 10D, where D is the orifice equivalent diameter) as the area of interest for the PIV calculations along with multi-pass interrogation with step 1 interrogation area of 64 × 64 pixels, step 2 window size 32 × 32 pixels and final window size 24 × 24 pixels, with 75% overlapping. Final resolution was about 0.5 vectors/mm, which meant 10 vectors each diameter length. PIV errors were assessed by computing the mean ratio between the amount of spurious vectors over their total number in each frame. Its maximum value was about 1%, but usually it was around 0.5%. Nevertheless, spurious vectors were replaced with interpolated ones during validation process by means of a local median filter (3-by-3 window and threshold equal to 3) and a standard deviation filter (threshold equal to 5). Moreover, the statistical error on average field is reduced by a factor related to the inverse of the square root of the number of images. Error bars were reported for mean axial velocity profiles in Fig. 5, in the manuscript. 95%-Confidence intervals were about ± 0.005U_0 for all jets. A similar value is derived also for mean velocity profiles at different jet cross sections. Eventually, about 5000 vectors were evaluated from each of the image pairs.

3. Results and discussion

In order to study mixing performances of plunging jets, we have investigated the following measures: axial velocity decay, potential (unmixed) core length [42], spreading rate (in terms of half-velocity width $y_{\frac{1}{2}}$) [11], ambient mass entrainment [43] and turbulence quantities (namely, rms profiles) [4].

Rectangular jets exhibit a phenomenon called “axis switching”, where major and minor axes of the jet cross-section are interchanged downstream of the orifice [14]. In the present case of a plunging jet, this phenomenon takes place as soon as the jet moves out in air, as reported in Fig. 3 for two side views and two top views of the event. After axis switching, the jet changes its shape by rounding the smaller sides of the rectangle and almost dividing the flow into an upper and lower main round-like jets. These are connected by a thin water sheet, which can be partially or fully eroded by them (depending on jet Reynolds number) before the impact with the free surface. In the former case, at the plunging point the jet draws an “8” shape footprint (Fig. 3a), meanwhile, in the latter, the 8-shape is elongated (Fig. 3c). The presence of a flat vertical sheet after the axis switching position was already observed by Lord Rayleigh [44] for an elliptic free surface jet, who distinguished between conditions for which multiple switching occur during the falling time and jets where only one switch happens. These different behaviours were explained mathematically by Bechtel and colleagues [45] for an elliptic jet in terms of the relative weight of the surface tension forces to the inertial and gravitational ones. Accordingly, as the former becomes weaker with respect to the others, the jet cross-section reaches a circular shape and then spreads into a ribbon in the plane normal to the orifice major axis. Thus, we can speculate that in our tests multiple switching was not observed for two main reasons:

1) for both low and high jet velocities, the free-falling path of the jet was too short;

2) for high velocities, where inertial forces become predominant over surface tension, the jet almost divided into two semi-round ones (after the first axis-switching) which do not allow axis-switching anymore.

3.1. Velocity fields

In Fig. 4 we report an example of the mean velocity magnitude for a circular plunging jet at Reynolds number about 11000 (a) and 25500 (b), and a rectangular plunging jet at Reynolds number about 13000 (c)

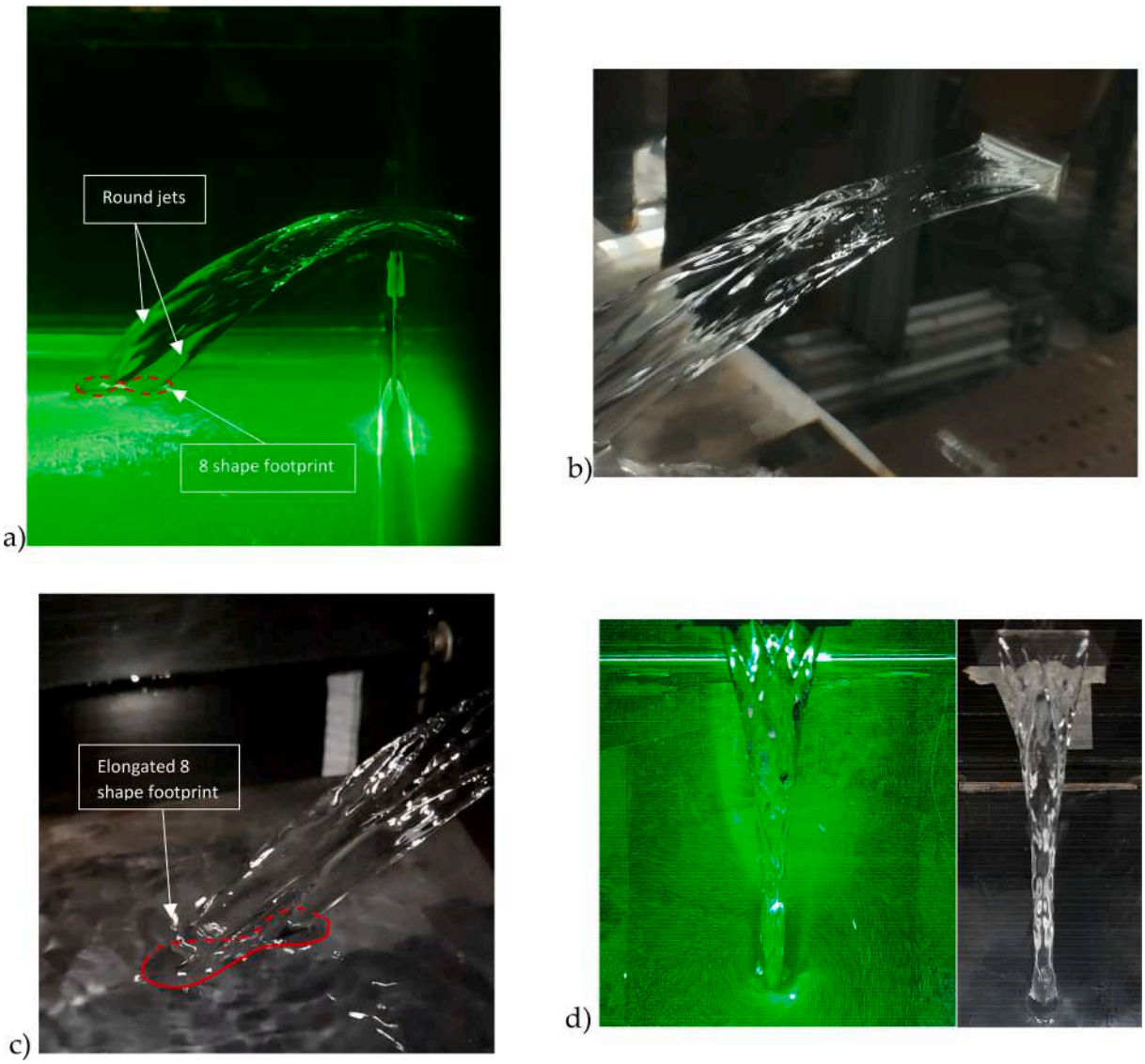

Fig. 3. Rectangular plunging jet views from: a) side, b) top-side detail of the plunging point, c) top-side, d) top. In a) we have pinpointed the round jets, and the footprint shape at the plunging point, while in c) an elongated "8" shape footprint is showed.

and 25000 (d). Magenta, white, black and cyan lines represent respectively the upper jet limit, the geometric centerline, the maximum velocity line and the lower jet limit. Jet limits are defined as the loci where the velocity magnitude reaches one-half of its maximum value (*i.e.* at the half-velocity width). Circular and square markers lay on equally spaced jet cross sections, with a step distance of one jet diameter. Velocity magnitude is made non-dimensional by the jet outlet velocity, as derived from flow rate measurements. Jet geometric centerline is derived as the mean positions between the jet limits.

Circular jets spread into water and the normalized velocity magnitude decreases from the jet cross section at an axial distance x/D=2, to the jet impact location on the bottom wall. Strictly speaking, however, the ratio U/U_0 remains greater than one for the first one diameter, due to the presence of the potential core which vanishes completely only far away. Jet boundaries show an increment of cross sections in streamwise direction. This is particularly evident for the lowest Reynolds number jet, thus suggesting a higher spreading rate in this condition. Moreover, maximum velocity line (i.e. the jet centerline) never overlaps to geometrical centerline, thus suggesting a non-symmetrical appearance of this jet in its entire length. Instead, as Reynolds number is increased, the two lines almost collapse earlier onto each other, from about one or two diameters downstream. Thus, an axisymmetrical shape of the jet is reached at these distances.

For rectangular plunging jets, the ratio between the velocity and the reference velocity U_0 is still decreasing in streamwise direction, but a clear double jet-like behaviour is visible for Reynolds number ≈25000. In comparison to circular jet's results, we observe a quite opposite behaviour of the jet centerline and geometrical axis. Indeed, they start to collapse onto each other at about x/D≈3 for Reynolds number ≈13000, while they are kept away along the entire jet length for Reynolds number ≈25000. Thus, in the latter case, we always can expect an asymmetrical shape of its cross sections. Jet boundaries seem to remain very straight as rectangular jets evolve downstream.

This suggests a smaller spreading rate of shear layers compared to circular plunging jets and thus a limited ambient fluid entrainment. As a matter of fact, jet centerline is always displaced towards the upper limit of the jet, both in circular and rectangular asymmetrical cases. Therefore, the upper part of the jet is always flowing faster than the lower part. We can speculate that this fact can be ascribed to their different falling height, whose range is $h \pm D/2$ (where h is the distance between the pool free surface and the center of the orifice). The latter let the upper part travel for a slightly longer time before plunging in the pool,

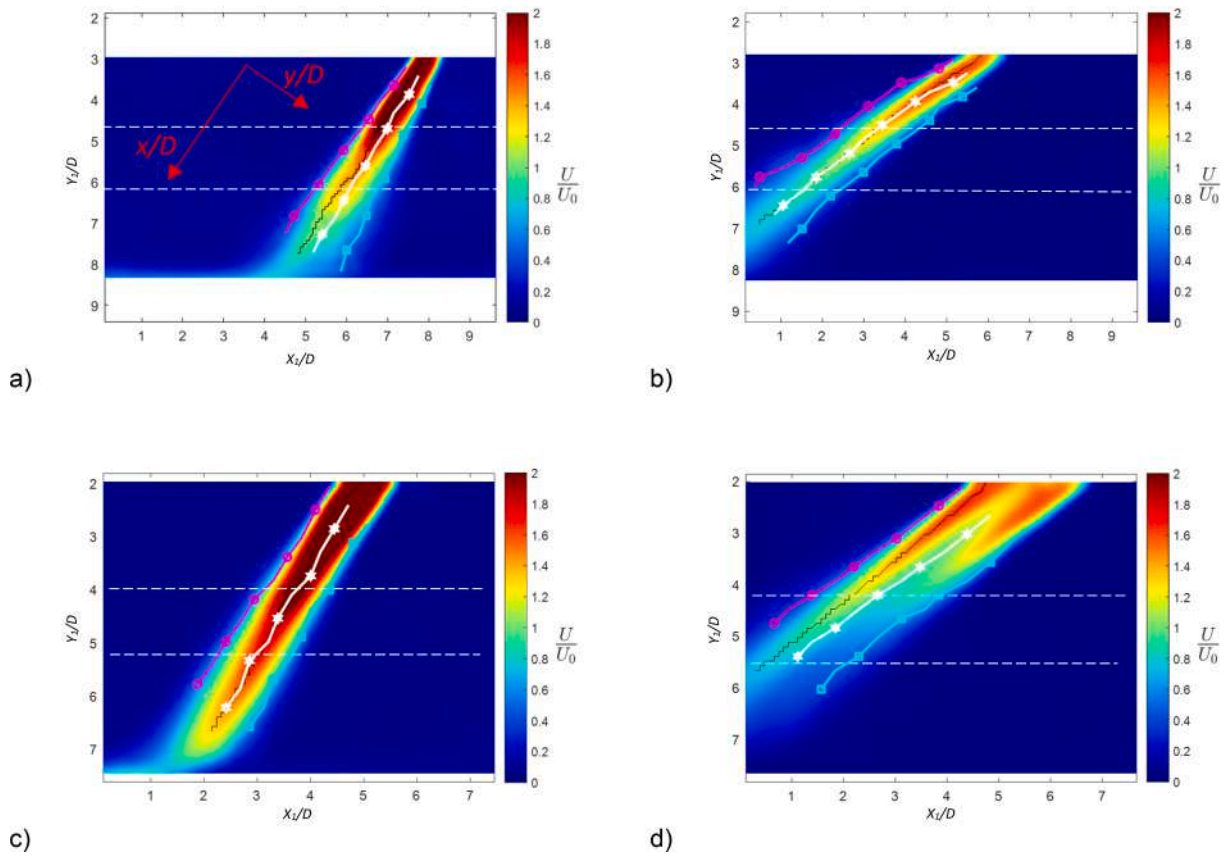

Fig. 4. Mean velocity field for a circular jet at (a) Reynolds number≈11000 and (b) Reynolds number≈25500, and a rectangular jet at (c) Reynolds number≈13000 and (d) Reynolds number≈25000. Topological loci are reported with lines of different colours: magenta and cyan lines indicate jet upper and lower limit respectively, black line is the jet axis (as derived from the loci of the maximum velocity), while white line is the geometric axis of the jet. Markers on each line lay on uniform-spaced jet cross sections with a step of 1 diameter. In (a), a new coordinate system of axes *x/D* (small "x", whose direction is parallel to the streamwise direction) and *y/D* (small "y", whose direction is normal to the streamwise direction) is reported in red. White dashed lines represent PIV horizontal measurement planes already showed and described in Fig. 1. (For interpretation of the references to colour in this figure legend, the reader is referred to the web version of this article.)

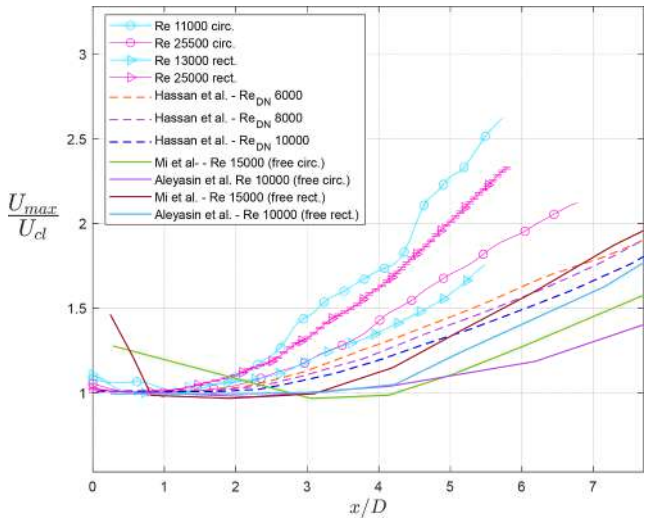

Fig. 5. Inverse of mean centerline velocity decays for circular and rectangular plunging jets, normalized by their maximum velocities. Representative literature results are reported for a circular vertical plunging jet [4] and two free circular and rectangular jets [1342]. Error bars related to 95% confidence intervals (of about $\pm 0.005U_0$) of the velocity are reported for rectangular jet at Reynolds number≈25000 and they are representative of all other jets' uncertainties.

so that it can reach a higher velocity at the plunging point (in agreement to a ballistic model presented below). Moreover, jet inclination angle (i.e., the angle between the jet centerline and the horizontal surface) depends on Reynolds number, such that it increases as Reynolds number is decreased. This behaviour can be ascribed to the competition between the inertial forces and the gravitational effects, so that a ballistic model can be used to describe quite well these jets. Inclination angle θ values are about 57° and 61° for circular and rectangular lowest Reynolds number jet, respectively, while they are ≈37° and ≈40° for circular and rectangular highest Reynolds number jet. Furthermore, θ seems to have an effect on the evolution of the two shear layers. Indeed, in circular jets, for great θ values, the lower shear layer is found to be the most enlarged, while for lower angle the upper layer grows faster. We can speculate that these different behaviours are due to the effect of the free surface and the orifice plate on the right-hand side of the jet. At high inclination angles, wall proximity creates a recirculating and an intense co-flow region in the lower part of the jet. Meanwhile, for lower inclination angles, free surface acts as previously done by the wall, thus producing an intense co-flow even in the upper part of the jet. These processes are reported and detailed in section 3.3.

Previous findings about the ratio U/U_0 are confirmed by axial velocity profiles both for circular and rectangular jets. In the former case, a higher velocity decay is observed for Reynolds number equal to 11000, reaching a value of U_{max}/U_{cl}≈2 at about x/D≈5 (where U_{max} is the greatest value of the mean velocity along the jet centerline; please, note the use of capital "X_1" and "Y_1" for horizontal and vertical direction respectively, and small "x" and "y" for parallel and perpendicular direction to the flow). Meanwhile, the same ratio is obtained about x/D≈7

for Reynolds number equal to 25500 (Fig. 5). In the latter case, the highest decay is obtained for Reynolds number≈25000 and decreases as Reynolds number decreases. Following Mi and colleagues [42] and Aleyasin and colleagues [46] approach, we define and compute the potential core length as the distance along the jet axis where the velocity reaches ≈98% of its maximum value. Moreover, by applying a linear model to the velocity decay as typically encountered in free jets [24,46]:

$$\frac{U_{max}}{U_{cl}} = K_u\left(\frac{x - x_0}{D}\right) \quad (1)$$

we derived the results reported in Table 2. Variables in eq.1 are maximum centerline velocity value U_{max}, centerline jet velocity U_{cl}, streamwise abscissa x, orifice diameter D and decay factor K_u. Higher K_u values are associated to a faster diffusion of the flow and a greater momentum exchange, thus suggesting a higher mixing. Potential core length in circular plunging jets is greater for higher Reynolds numbers and has a value of approximately 2.5D for the highest Reynolds number, while it's ≈1.6D for the lowest one. At the same time, linearity starts at a distance of about 2 diameters beneath the plunging point and ends after 3.5 diameters due to the pool floor effect for Reynolds number equal to 11000. Meanwhile, the longer extension of potential core results in a delayed onset of the linearity for higher Reynolds numbers. Faster velocity decay is obtained for lower Reynolds numbers, while the lowest value of K_u≈0.24 is gained for Reynolds number≈25500 jet.

Rather, rectangular plunging jets reveal a potential core length whose smaller value is ≈1.5D and is derived for the highest Reynolds number, which also exhibits the highest slope K_u≈0.35 (Table 2). Higher Reynolds numbers have higher velocity decays and lower potential core lengths, thus suggesting better mixing properties, in contrast to previous findings of circular jets.

Free jets literature results are also reported in Table 2. They show longer potential core length for all considered Reynolds numbers, smaller velocity decays and a wider linearity region. This is confirmed by the results of Hassan and colleagues [4], who found that the potential core length should fall within a range of about x/D=1.82–2.78 for a vertical circular plunging jet and Reynolds number between 4000 and 10000. In our study, we found a length interval between 1.6 and 2.0 for circular plunging jet depending on Reynolds number, which is even smaller for rectangular plunging jets. This fact, along with the greater velocity decays reported in Fig. 5, suggests that an inclined plunging jet has a faster momentum exchange than vertical plunging jets and free jets. Therefore, it has an enhanced mixing ability. Indeed, we observe that for inclined jets there is a horizontal velocity component which is not present in vertical ones, whose relative magnitude (with respect to the constant gravitational component equal to $\sqrt{2gh}$, as derived from eq. (3)) becomes greater as the inclination angle decreases. This velocity component points outward for fluid in the upper part of the jet and inward for fluid in the lower part. Therefore, the momentum exchange with the ambient (slower) flow occurs not only due to Kelvin-Helmholtz instability and jet spreading (as for vertical jets), but also thanks to the contribution of this horizontal velocity component. As a result, we obtain a faster momentum exchange.

Table 2
Potential core length and linear approximation results for present circular and rectangular plunging jets and free jets from literature.

Orifice	Re_D	Potential core end [x/D]	K_u	Linear from-to [x/D]
Circular	11000	1.6	0.40	2 to 3.5
Circular	18000	2.0	0.39	2 to 5
Circular	25500	2.0	0.24	2.5 to 6
Rectangular	13000	2	0.15	2 to 4
Rectangular	15000	2	0.166	2 to 4.5
Rectangular	19000	2	0.30	2.5 to 5
Rectangular	25000	1.5	0.35	2.5 to 6
Mi et al. [42] – free round jet	15000	4,2	0,208	11 to 40
Hashiehbaf et al. [24] – free round jet	8000	4,25	0,185	6 to 20
Aleyasin et al. [13] – free round jet	10000	3,8	0,171	10 to 30
Aleyasin et al. [13]- rectangular free jet	10000	3.4	0.192	10 to 30
Mi et al.[42] – rectangular free jet	15000	3.1	0.202	8 to 40

Furthermore, by comparing circular and rectangular plunging jet's results, we derive that highest decay is shown in the former jets for low Reynolds number, while it belongs to high Reynolds number jets in the latter. Another result of Fig. 5 is the close behaviour of circular jet at Reynolds number≈25500 and rectangular jet at Reynolds number≈13000. They almost collapse onto each other until x/D≈5.3, where the latter starts to diverge. Therefore, from axial velocity decay point of view, these two jets are equally the worst ones in terms of mixing properties when compared to the other investigated jets.

Half-velocity width profiles are evaluated on mean velocity magnitude maps, with an error range of ±0.07D for circular jets and ±0.06D for rectangular jets. They point out a trend in the upper part of those jets which is similar for all Reynolds numbers and orifices, showing an approximately linear increase (Fig. 6a). Meanwhile, in the lower part, there is a clearly different behaviour of the half-velocity width for the two jet's geometries. Circular lower-part width always increases in streamwise direction. The steepest increment is observed for Reynolds number 11000 (Fig. 6a), while trends become flatterer as Reynolds number is increased. This suggests a major spreading rate of the lowest Reynolds number case in respect to the higher ones, which in turn seem to evolve more axisymmetrically. On the other hand, rectangular lower-part width decreases till a minimum after which it rises again (Fig. 6b). Lower part rectangular values are greater than the corresponding circular ones; this may be attributed to the axis switching phenomenon, which has stretched the jet mostly onto one plane (the vertical one in Fig. 1), where it shows an asymmetrical velocity distribution (Fig. 4), and it is not necessary related to a higher entrainment. Indeed, by looking at the growth rate of the upper half-velocity width, we find that values are generally close to the corresponding circular plunging jets, which suggests the same spreading ability. Nevertheless, the decreasing tendency of rectangular lower half-velocity widths can be associated to an early vanishing of the lower round jet (see the jet configuration in Fig. 3a, which is still appreciable for low Reynolds number jets) with respect to the upper one. Moreover, as it will be described in section 3.4, high Reynolds number jets exhibit a counter-clockwise rotation of their cross sections, so that their lower part is no longer observable on the central vertical plane after some diameters downstream.

Transverse circular velocity magnitude profiles show a Gaussian-like shape for all the cross-sections even though the effect of the pool floor modifies the shape for Reynolds number equal to 11000 after x/D≈5 (Fig. 7). An asymmetric behaviour is clearly visible for all jets, but it becomes less evident as the jet moves downstream. The maximum velocity ratio U/U_0 is always reached at x/D≈1 after which it remains constant or decreases, while the Gaussian shape increases its width. This confirms the spreading behaviour of the jets and the thicker cross section in lower Reynolds number cases. However, as the Reynolds number is increased, the maximum non dimensional velocity value decreases from ≈2.4 for Reynolds number 11000, to ≈1.6 for Reynolds number 25500. This is consistent with a ballistic modelling of the jets before plunging onto the free pool surface:

$$t_{fall} = \sqrt{\frac{2h}{g}}, \quad (2)$$

$$U_{yfall} = g\Delta t \quad (3)$$

$$\frac{U_{pp}}{U_0} \approx \sqrt{1 + \frac{U_{yfall}^2}{U_0^2}} = \sqrt{1 + \frac{2gh}{U_0^2}} \quad (4)$$

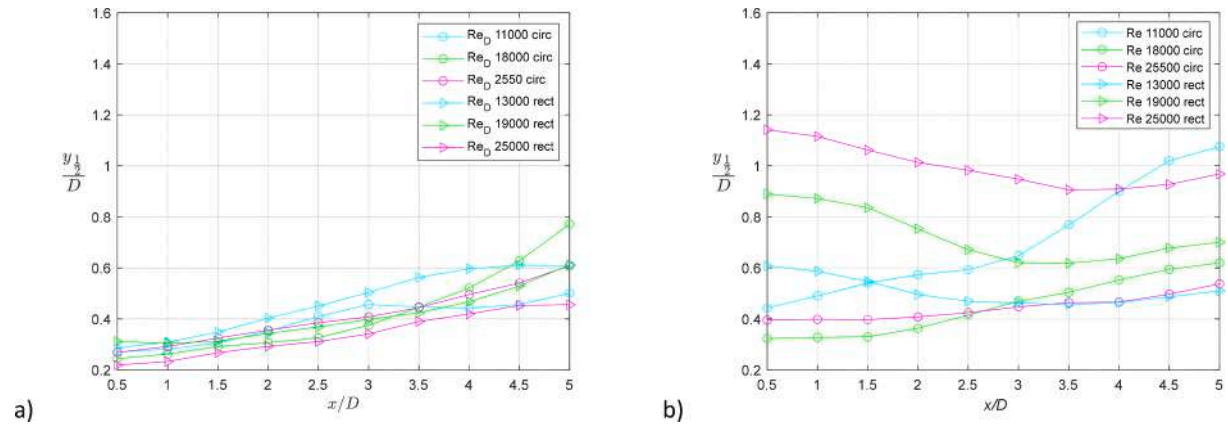

Fig. 6. Half-velocity width profiles normalized by the orifice's diameter D: a) upper part of the jet; b) lower part of the jet; please, note that $y_{1/2}$ values have been evaluated with an error range of ±0.07D for circular jets and ±0.06D for rectangular jets.

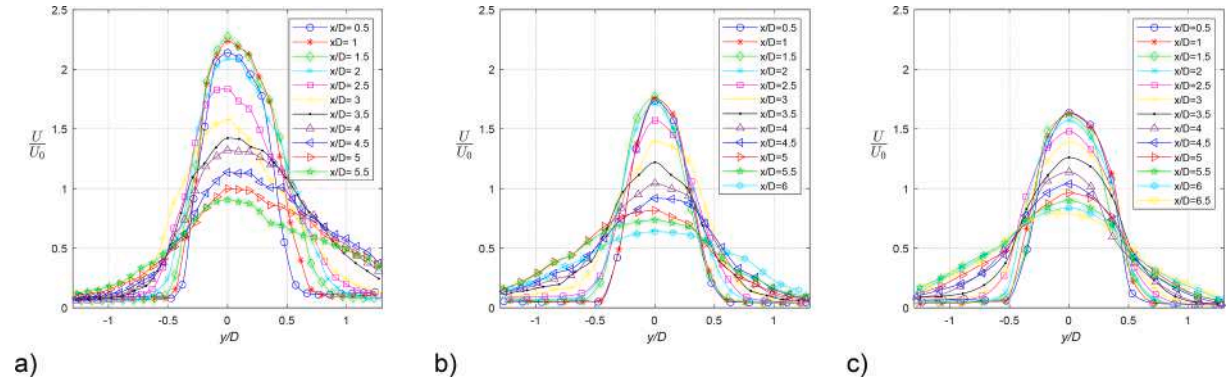

Fig. 7. Transverse velocity magnitude profiles of circular plunging jets at different cross-sections for a) Re_D≈11000, b) Re_D≈18000 and c) Re_D≈25500. Velocity is normalized by the velocity as derived from the flow rate measurement. 95% confidence intervals have same order of magnitude as the ones of Fig. 4, so that they are not reported here. (For interpretation of the references to colour in this figure legend, the reader is referred to the web version of this article.)

where t_{fall} is the falling time of the jet, Δt is t_{fall}-t_0, t_0 is the starting falling time (assumed equal to 0), h is the vertical distance between the orifice and the pool free surface (≈3.5D), U_{yfall} is the vertical component of the velocity at the plunging point due to gravity g and U_{pp} is the velocity magnitude at the plunging point by neglecting losses due to friction between water and air. Please, note that we consider the flow to have only a horizontal velocity component at the orifice outlet (which is equal to U_0), while U_{pp} is computed as the resultant of U_0 and U_{yfall}. In Table 3 we report an estimate of the ratio U_{pp}/U_0 as derived both from a ballistic model and our experimental data. These values are quite in agreement. Their differences are in the order of 1–13% (greater values are associated to higher Reynolds number jets).

Transverse velocity profiles of rectangular jet show that, as the jet expands downstream, it moves towards a Gaussian shape, with the second peak that vanishes further downstream as Reynolds number is increased (Fig. 8). A more symmetrical behaviour is observed after x/D≈3 for Reynolds numbers 13000 and 15000, while it's never reached along the jet length in the other cases. However, we can conjecture that also in those latter cases a more symmetrical profile would be reached, but it requires a longer distance to dissipate the greater energy content of the upper jet as compared to the lower one. As Reynolds number is increased, asymmetry becomes more evident in rectangular jets due to a larger spreading of their cross sections after the axis switching point. Indeed, upper jet has a higher falling range and time before plunging in the pool, thus can reach higher velocities. Moreover, the double jet-like configuration leads to the presence of four shear layers (two for both the upper and lower jet) so that a turbulent region rises between the two jets and can increase mixing. Velocity ratio U/U_0 is greater for lower Reynolds numbers and it is about 2.2 for Reynolds number 13000, while it is only 1.6 for Reynolds number 25000. This is consistent with eq.4 estimate.

Even though self-similarity behaviour is typically encountered in round free and vertical plunging jets [184], it is not observed in our tests.

Table 3
Evaluation of the ratio U_{pp}/U_0 as derived from a ballistic model and current experimental data.

Orifice	Re_D	U_0 [m/s]	Ballistic model - U_{pp}/U_0	Experimental data - U_{max}/U_0
Circular	11000	0.53	2.42	2.40
Circular	18000	0.84	1.72	1.80
Circular	25500	1.19	1.40	1.58
Rectangular	13000	0.59	2.22	2.25
Rectangular	15000	0.66	2.03	2.16
Rectangular	19000	0.88	1.66	1.81
Rectangular	25000	1.14	1.44	1.65

3.2. RMS profiles

Starting from the velocity field, horizontal and vertical velocity components, u and v, are reprojected orthogonally and along the jet axis thus obtaining axial and radial velocity components, namely u_{reproj} and v_{reproj}. Then, their temporal mean values are subtracted thus obtaining their fluctuations. Therefore, fluctuations' centerline rms values are computed and reported in Fig. 9 for circular and rectangular orifice

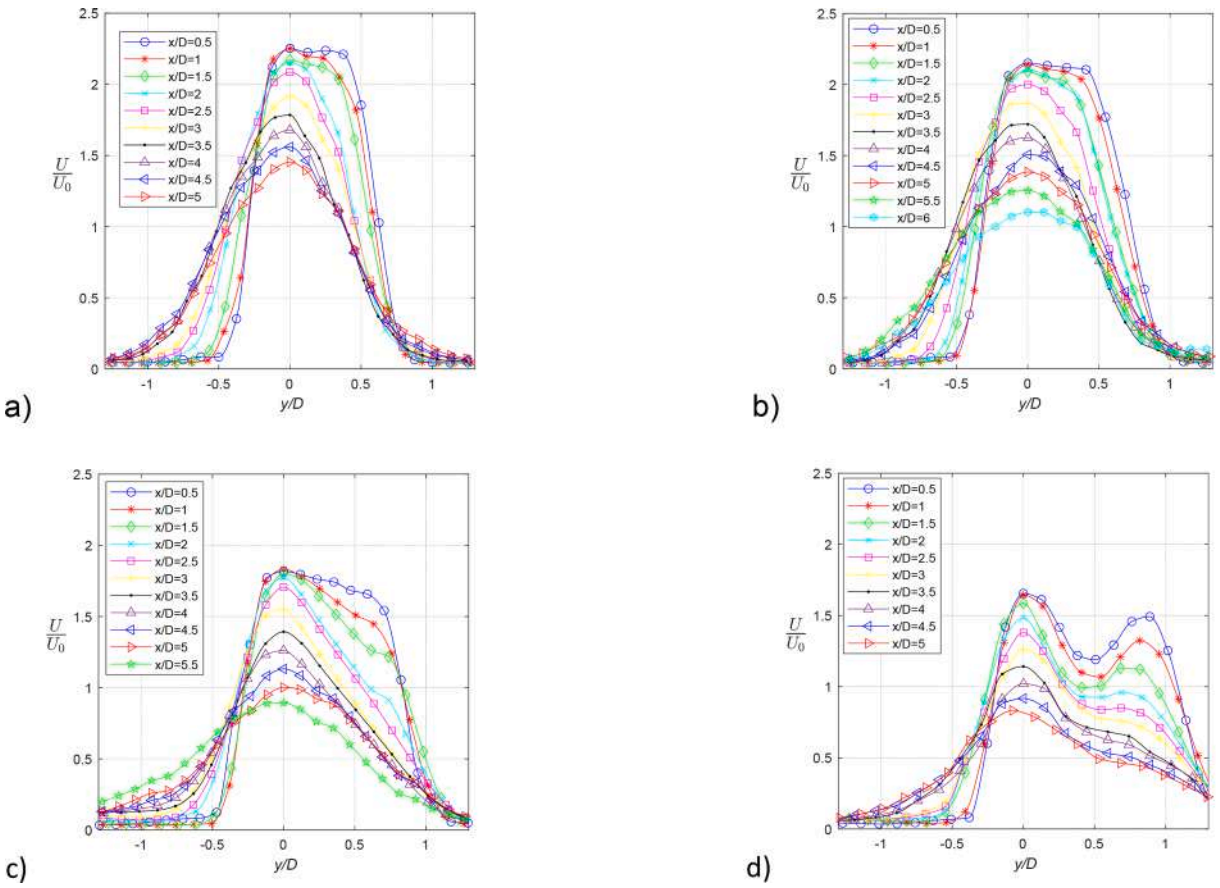

Fig. 8. Transverse velocity magnitude profiles for rectangular plunging jets at different cross-sections for a) $Re_D \approx 13000$, b) $Re_D \approx 15000$, c) $Re_D \approx 19000$ and d) $Re_D \approx 25000$. Velocity is normalized by the velocity as derived from the flow rate measurement. 95% confidence intervals have same order of magnitude as the ones of Fig. 4, so that they are not reported here. (For interpretation of the references to colour in this figure legend, the reader is referred to the web version of this article.)

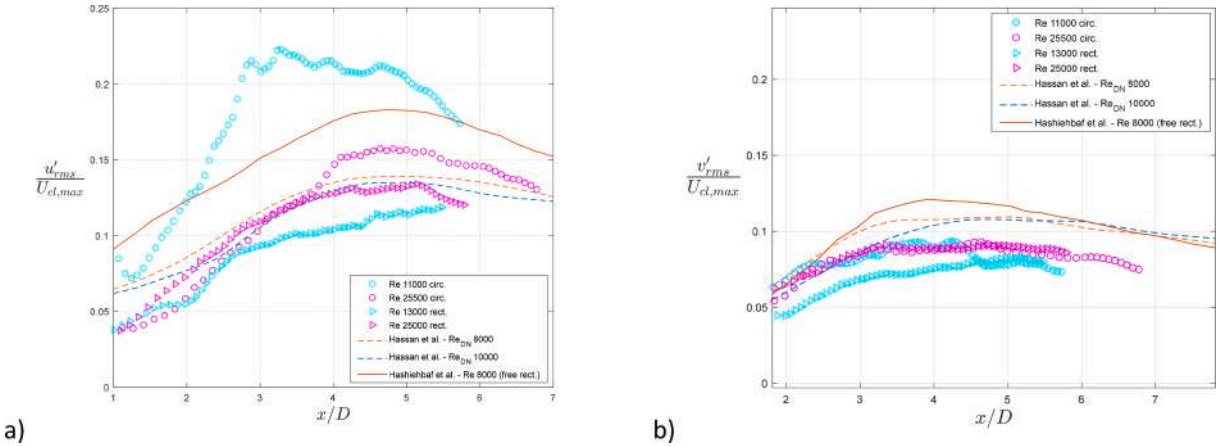

Fig. 9. RMS profiles of u' (a) and v' (b) fluctuations of the jet centerline velocity as reprojected respectively along and normally to the jet axis. Literature results are reported for a circular vertical water plunging jet [4] and two rectangular free water jets [24].

geometries and Reynolds number equal to 11000–25500 (circular jet) and 13000–25000 (rectangular jet). Circular u' rms component is greater for lower Reynolds numbers and peaks earlier than in higher Reynolds number jets. This confirms the greater momentum exchange of these jets, which leads to a faster dissipation of the potential core, a higher turbulent production and thus a better mixing. Indeed, the rise of fluctuations' rms values is associated to the vanishing of the potential core region and closure of shear layers, which leads to an increase in the turbulence production [4]. Strictly speaking, there is an almost linear rising tendency in the very near field till a certain distance below the plunging point, followed by a decreasing region. This behaviour is consistent with previous studies on free jets [21,47,48]. Turbulent production is pointed out by power spectra distribution for both circular and rectangular jets, as reported in Fig. 10 and Fig. 11. They are evaluated at two axial locations (i.e. x/D=2 and x/D=4) along jets' maximum line and at half-velocity width boundaries. All jets reach a fully developed turbulent condition along their centerlines in streamwise direction, and their trends are found to approximate the $f^{-5/3}$ law

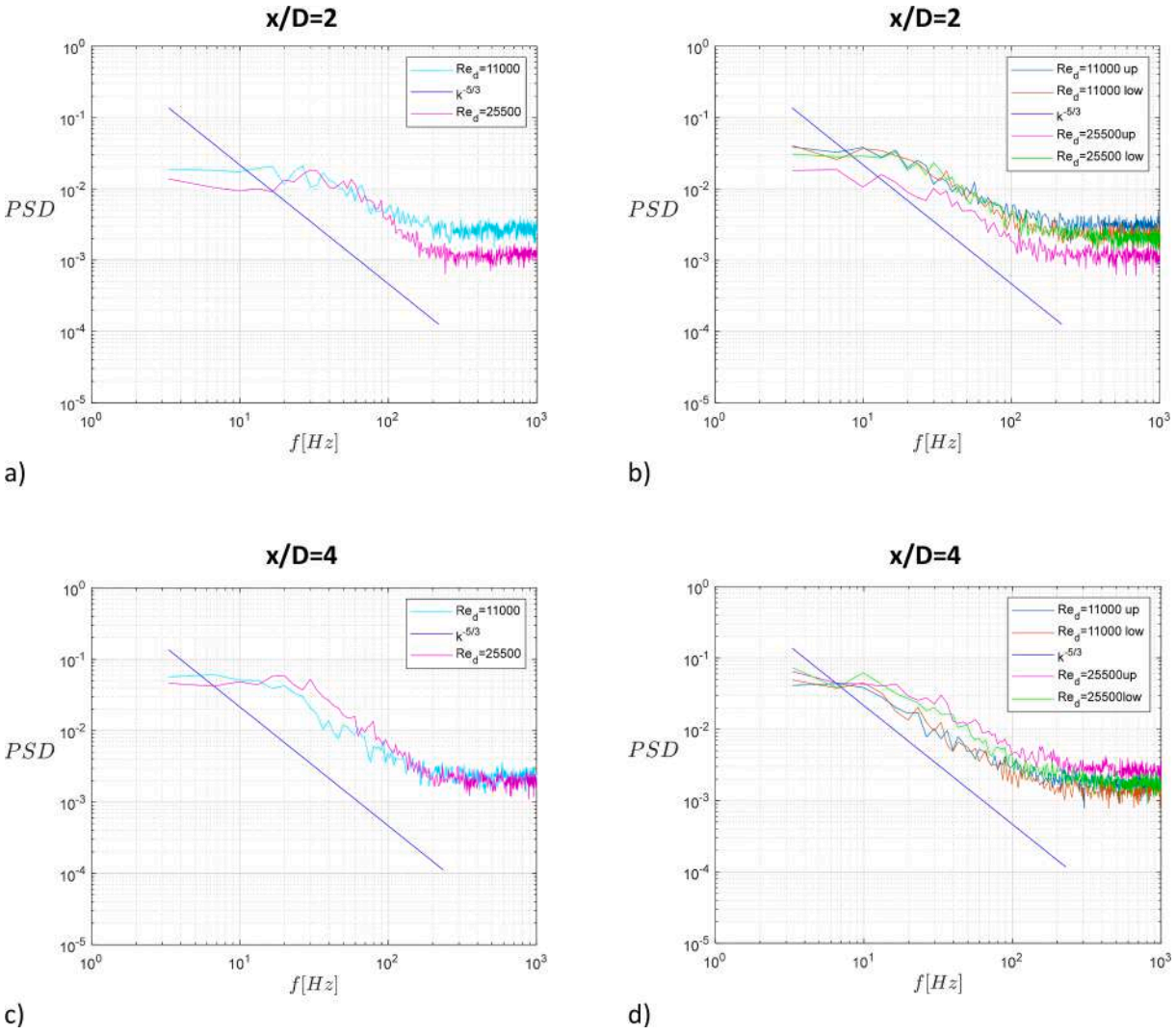

Fig. 10. Power spectra for a circular jets at x/D = 2 (a,b) and x/D=4 (c,d), along the jet centerline (a,c) and at half-velocity width locations (b,d), for Re_D=11000 and Re_D=25500. (For interpretation of the references to colour in this figure legend, the reader is referred to the web version of this article.)

[49] in the inertial range since x/D≈2, even though the lowest Reynolds number circular jet require a longer axial distance to match that profile (x/D≈3). Meanwhile, speaking about spectra at y1/2, they do not show any clear difference between the upper and lower part of the jets, their trends are quite in agreement to the centerline ones in the entire frequency range.

By comparing circular rms growth rates with what reported by Hassan and colleagues [4] for a vertical round plunging jet, they are generally higher and show a peak value at Re_D=25500 that approaches the one of a free rectangular jet at Reynolds number equal to 8000 [24]. Thus, circular bended plunging jets exhibit better mixing performances than both free and vertical plunging jets. As a matter of fact, axial rms profiles of our rectangular jets are always lower than the corresponding circular ones, even though both the highest Reynolds number cases reveal a close behaviour until x/D≈3. Rectangular plunging jets have an initially linear rising profile too, slightly steeper than those of vertical round plunging jets [4], and qualitatively similar to what Hashiehbaf and Romano [24] showed for a rectangular free jet. At about x/D≈3, they reduce their growing rate and become more stable. In the highest Reynolds number case, values approach Hassan and colleagues [4] results, while in the lowest one they keep increasing less steeply. A similar behaviour is observed also for radial rms components both in circular and rectangular jets. This time, the growth is less steep in the first part of the jets and, after x/D≈3, it's almost vanishing. Interestingly, circular jets and the highest Reynolds number rectangular jet are almost overlapping in streamwise direction, while the lowest Reynolds number rectangular jet shows slightly lower values, reaching the others only far away, at x/D≈5-6. All tested plunging jets show a small plateau region after the initial rising zone, from where they start to decrease. However, these results point out that there are no clear differences in turbulent production between the two jet geometries in normal direction.

3.3. Ambient mass entrainment

Following Ricou and Spalding [50], mean flow rate is expressed by the streamwise velocity u_{reproj} and the radial distance y through the formula:

$$Q = \pi \int_{y_{\frac{1}{2}low}}^{y_{\frac{1}{2}up}} \left(\overline{u_{reproj}}\right) y dy; \tag{5}$$

where the over bar denotes a time-mean and the integration limits are chosen as the jet boundaries. However, in order to have a deeper understanding of the separate contribution of the upper and lower shear layers, the former integral is divided into two terms:

$$Q = \pi \int_{y_{\frac{1}{2}low}}^{y_{\frac{1}{2}up}} \left(\overline{u_{reproj}}\right) y dy = \pi \int_{0}^{y_{\frac{1}{2}up}} \left(\overline{u_{reproj}}\right) y dy + \pi \int_{0}^{y_{\frac{1}{2}low}} \left(\overline{u_{reproj}}\right) y dy; \tag{6}$$

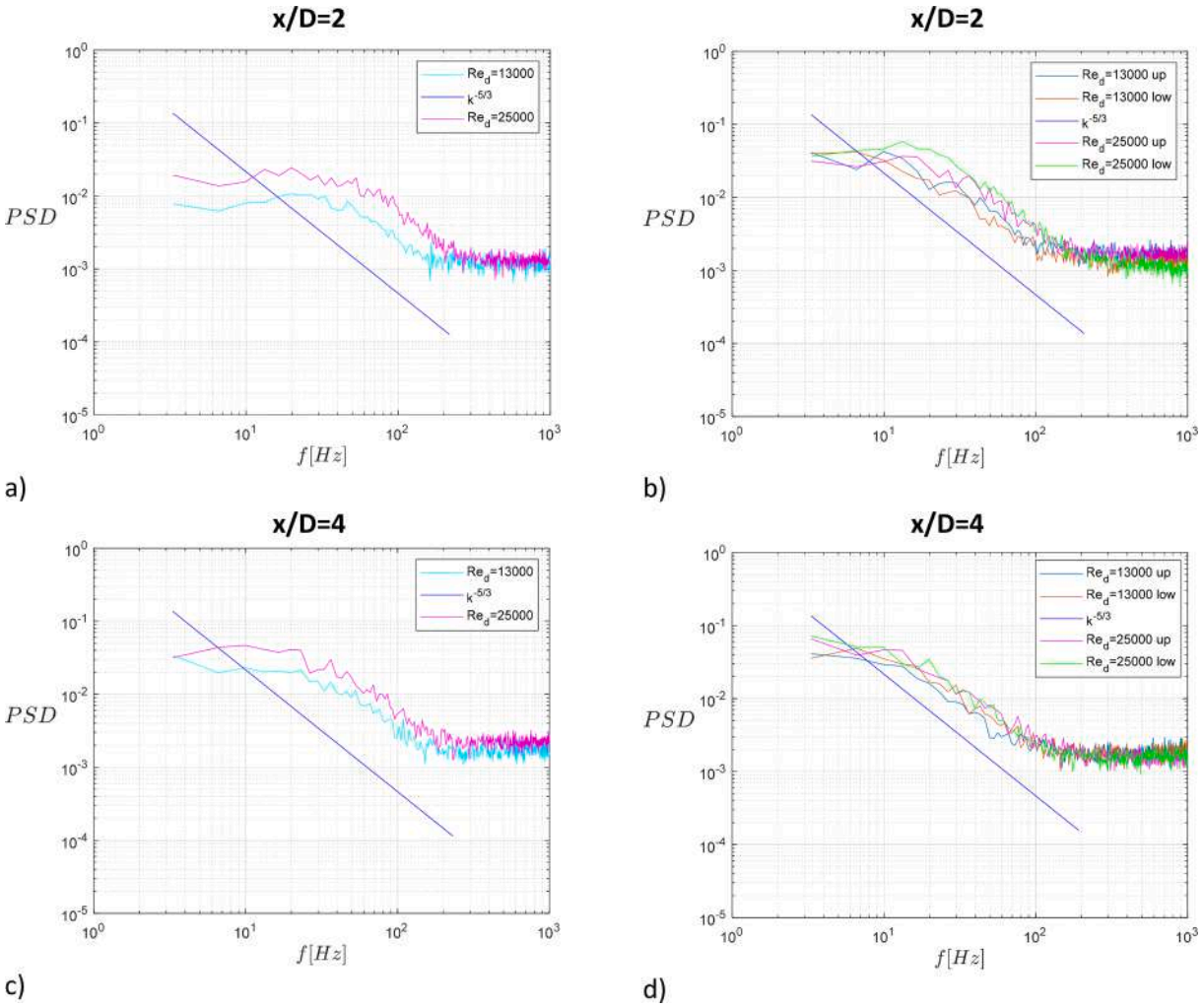

Fig. 11. Power spectra for a rectangular jets at x/D = 2 (a,b) and x/D = 4 (c,d), along the jet centerline (a,c) and at half-velocity width locations (b,d), for Re_D=13000 and Re_D=25000. (For interpretation of the references to colour in this figure legend, the reader is referred to the web version of this article.)

$$Q = Q_{up} + Q_{low} \tag{7}$$

Circular flow rate shows an increasing tendency for all considered Reynolds number in the near-field (Fig. 12a). The highest value is reached for Reynolds≈11000, even though from x/D≈5 it starts to be clearly affected by the confinement effect of the pool floor and decreases. Meanwhile, for Reynolds number equal to 18000 and 25500, profiles collapse almost onto each other. Similar results are obtained for ambient mass entrainment rate. It is computed as the derivative of the flow rate with respect to the streamwise direction and it is reported in

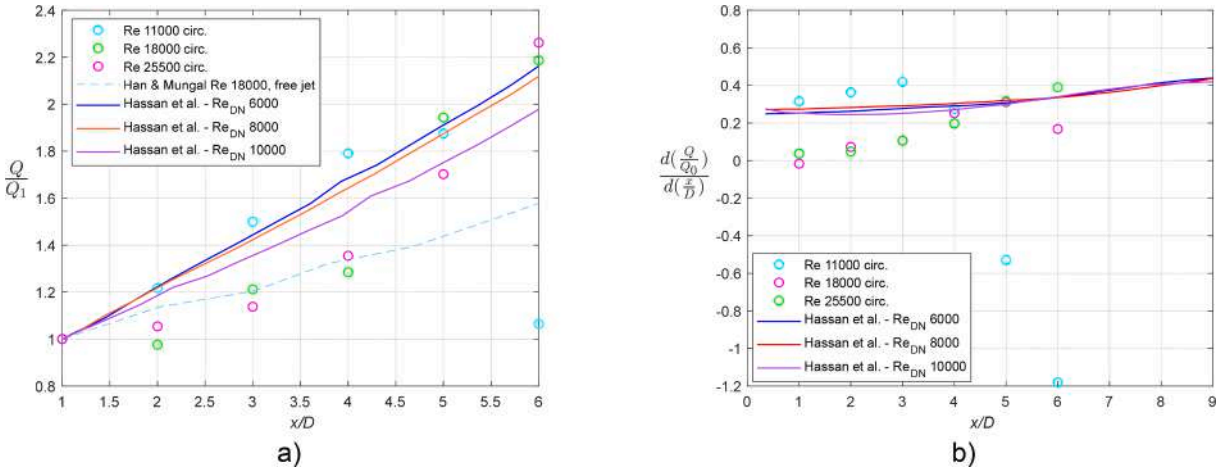

Fig. 12. (a) Mean total flow rate for circular plunging jets, normalized by flow rate at section x/D=1 and (b) mean entrainment rate. Literature results of a vertical plunging jet and a free jet are reported for comparison.

Fig. 12b for circular plunging jets. The lowest Reynolds number jet entrains the most till x/D≈4, from which it starts to decrease due to the bottom wall effect (the same trend is showed by the intermediate Reynolds number jet, but the decrease is delayed at x/D≈5). As a matter of fact, the highest entrainment rate values are associated to the lowest Reynolds number jet, thus confirming the previous findings of the half-velocity width on the jet enlargement, the axial velocity profiles and the potential core closure. Therefore, we can expect a greater turbulent and mixing production by this jet. In Fig. 12a and Fig. 12b we have reported literature results of a vertical round plunging jet [4] and a free round jet [51] for comparison. Even though they used a different criterion to identify the jet boundaries, we can still compare their results to ours by referring both of them to their values at x/D=1. Trends are similar, but our circular plunging jets entrain more ambient fluid at Reynolds number equal to 11000.

Rectangular mean flow rate behaviour points out an initial decreasing tendency till a minimum, from which it rises back to a percentage of its initial value (Fig. 13). This is observed for all Reynolds numbers, excepting for the highest one. Minimum positions and values, along with the recovery percentage, seem to be related to the Reynolds number itself, so that the higher the Reynolds number, the lower is the minimum value, the farther is its position and the lower is the recovery.

By dividing the single contribution of the lower and upper part of the jets, we can confirm half-velocity width previous findings. Indeed, circular upper shear layer shows an increasing trend in streamwise direction, even though for Reynolds number equal to 11000 it starts to slightly decrease after x/D≈3 (Fig. 14a). Rectangular upper shear layers have an increasing trend too and the steepest is observed for low Reynolds number cases (Fig. 14b). At the same time, circular lower parts of the jets give a flatter contribution to the ambient entrainment, excepting for the lowest Reynolds number jet (Fig. 14a). This is characterised by the increase of Q_{low} till about x/D≈5, after which it is affected by the confinement effect of the pool floor. Eventually, total mass flow rate belongs mostly to the lower part of the jet at the beginning, while it's more fed by the upper part in the last cross sections. In rectangular jets, lower contributions are always reducing and the greatest decreasing rate is associated to the highest Reynolds number (Fig. 14b).

These trends can be explained by looking at the mean velocity streamlines reported in Fig. 15 for circular jets at Reynolds number equal to 11000 and 25500. In the former case (Fig. 15a), the upper part of the jet is characterised by the presence of streamlines in the downhill region (i.e. region between the submerged jet and the outlet of the plunging pool) which indicate an entraining flow from the surrounding along the entire jet evolution. However, this behaviour seems to be

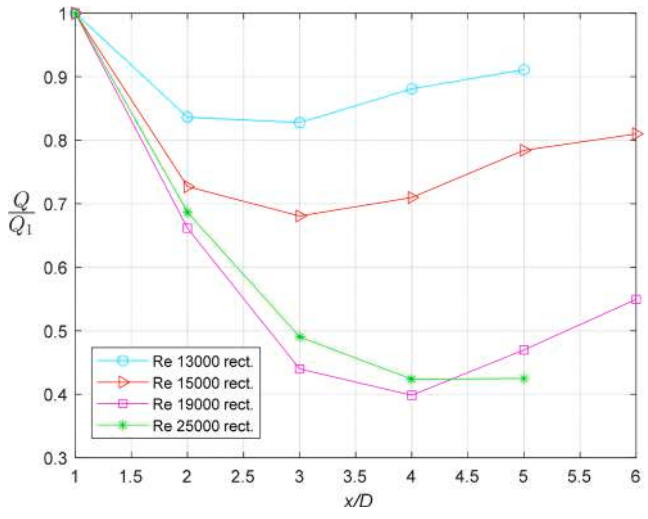

Fig. 13. Mean total flow rate for rectangular plunging jets, normalized by flow rate at section x/D = 1.

Reynolds number dependent, so that in the latter case (Fig. 15b) the entraining region is limited only to an area immediately below the plunging point, while surrounding fluid behaves more like a co-flow for the rest of the jet. Highest Reynolds number jet is characterized by the highest velocity, the lowest inclination angle and thus the shortest free cross distance between the upper part of the jet and the free surface. This can lead to a more intense recirculating region than the one of lower Reynolds number jets in the downhill, thus explaining the co-flow previously observed. At the same time, by focusing on the lower part of circular jet at Re_D≈11000, we find an increasing trend of the flow rate probably due to the presence of another co-flow, localized in the uphill region (i.e. region between the orifice plate and the submerged jet), owing to the proximity of the orifice plate. Moreover, lower part flow rate values are always greater than the those of other circular jets. A possible reason for this result can be the asymmetry, which is dominant along all the entire jet and always in favour of the lower part. Meanwhile, for greater Reynolds numbers, where asymmetry vanishes after some diameters downstream, values of both half-velocity widths and local flow rates in the upper and lower part of the jet are closer to each other. Eventually, high Reynolds number circular jets show, in their lower part, streamlines of entraining ambient fluid till a distance at which the presence of a vortex in the bottom-right of the uphill region (as a result of the orifice plate's confinement effect) deviates ambient flow, prevents its capture by the jet and creates another ambient co-flow.

Similar considerations can be done for rectangular jets. Streamlines reported in Fig. 16 a) and b) suggest an ambient entraining flow in the upper part of the jet for the lowest Reynolds numbers, and the presence of a co-flow in the lower part. Indeed, in Fig. 16a in the uphill, a recirculation region due to orifice plate confinement effect is clearly visible. Instead, in the highest Reynolds number case, upper part of the jet is characterized by a co-flow, while the lower one reveals the presence of a recirculation close to the shear layer, which can contribute to the diminishing of the flow rate in streamwise direction.

3.4. Horizontal planes

In order to study the three-dimensional effect of the jets, two horizontal planes are investigated: the first one is located at a height of about 7 cm (plane 1, Y_1/D≈3.5) from the pool floor, while the second one is at about 4.5 cm (plane 2, Y_1/D≈2.25). Owing to the different jet inclination by changing the Reynolds number, these planes cut the jets in different positions along the centerline.

Recalling the jet boundaries definition for vertical planes, they were derived again as the loci where the velocity is equal to a half of its maximum value. In Fig. 17 we report two examples for circular plunging jets at Reynolds number ≈11000 and Reynolds number ≈22000. Looking at those pictures, we observe that the jet footprint area is always increasing by increasing Reynolds number. This is consistent with the mathematical expression of the jet diameter at the plunging point due to the mass balance law:

$$Q_0 = U_0 A_{orifice} = U_{pp} A_{pp}; \tag{8}$$

$$\frac{U_{pp}}{U_0} = \left(\frac{D}{d_{pp}}\right)^2; \tag{9}$$

$$\frac{d_{pp}}{D} = \sqrt{\frac{1}{\sqrt{1+\frac{2gh}{U_0^2}}}}; \tag{10}$$

where U_0 is the velocity as derived from the flow rate measurements, U_{pp} and A_{pp} are respectively the normal velocity and the jet cross section area at the plunging point, h is the vertical distance between the orifice and the pool free surface. Please, note that U_{pp} expression in eq.10 was derived from eq. (4).

From the vertical plane velocity fields, we evaluate the ratio U_{pp}/U_0.

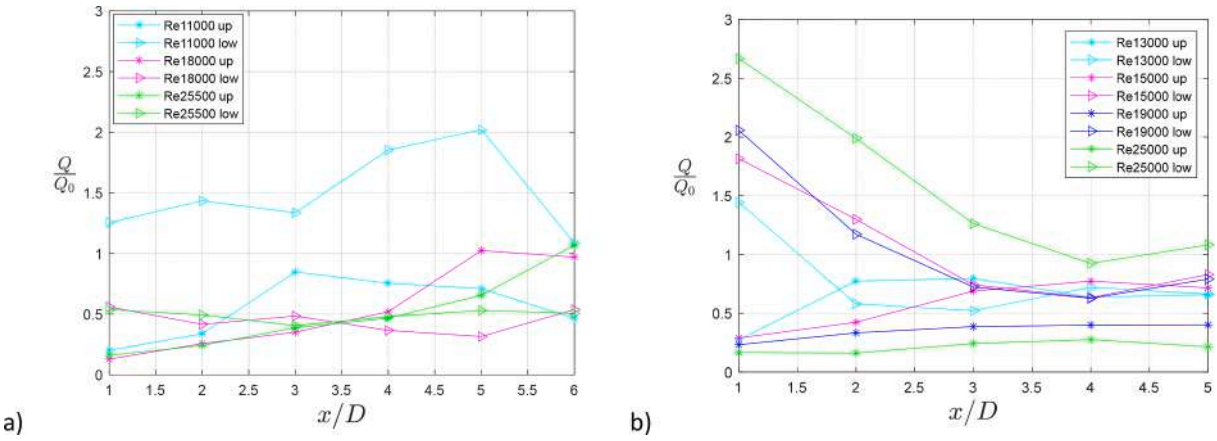

Fig. 14. Upper and lower contribution to the total flow rate normalized by the measured flow rate. Star and triangle markers are used respectively for Q_{up} and Q_{low} (as derived from eq.7) in a) circular plunging jets; b) rectangular plunging jets.

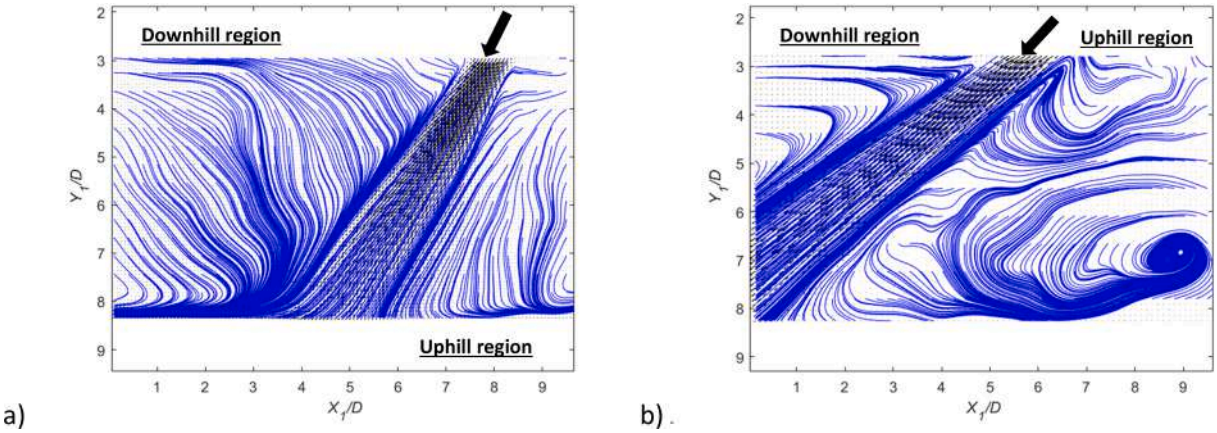

Fig. 15. Mean velocity circular jet streamlines for a) $Re_D \approx 11000$ and b) $Re_D \approx 25500$; small black arrows are mean velocity vectors, while the bigger one on the top of both images indicates the flow main direction. (For interpretation of the references to colour in this figure legend, the reader is referred to the web version of this article.)

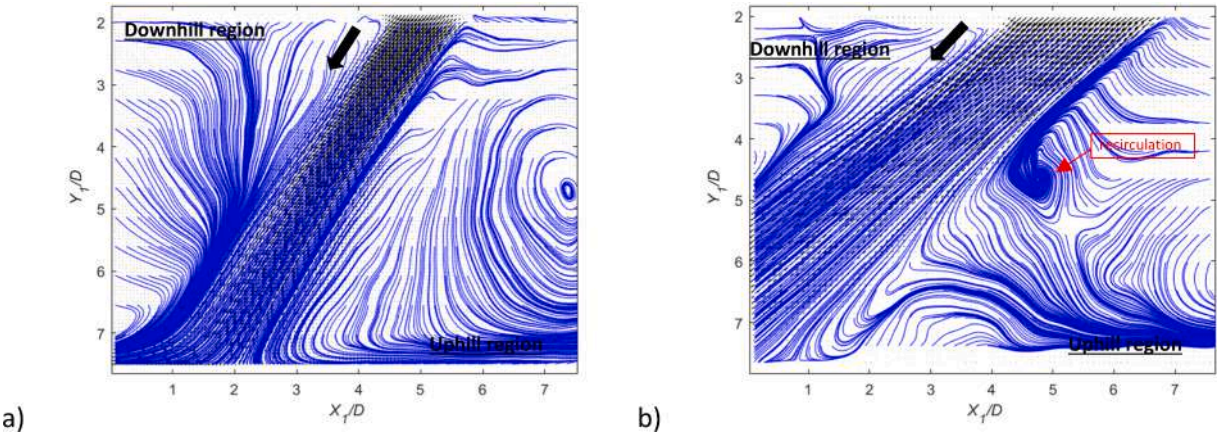

Fig. 16. Mean velocity rectangular jet streamlines for a) $Re_D \approx 13000$ and b) $Re_D \approx 25000$; small black arrows are mean velocity vectors, while the bigger one on the top of both images indicates the flow main direction. The presence of a vortex in the mean field close to the lower shear layer in b) can contribute to the diminishing of the flow rate in streamwise direction. (For interpretation of the references to colour in this figure legend, the reader is referred to the web version of this article.)

This value is about 2.4 for Reynolds number 11000 and 1.6 for Reynolds number 25500. Thus, we expect a greater d_{pp} in the latter case, about 1.2 times the one of former, which is confirmed by the horizontal plane measurements. As a matter of fact, we found that the greater the Reynolds number, the greater is the velocity U_0, the greater is d_{pp} and the smaller is U_{pp}/U_0.

Results of rectangular plunging jets show a counter-clockwise rotation of the jet cross section between the two horizontal planes heights (Fig. 18). Meanwhile, it was not observed for any of circular jets. It can be explained as a confinement effect of the pool that can be related to a

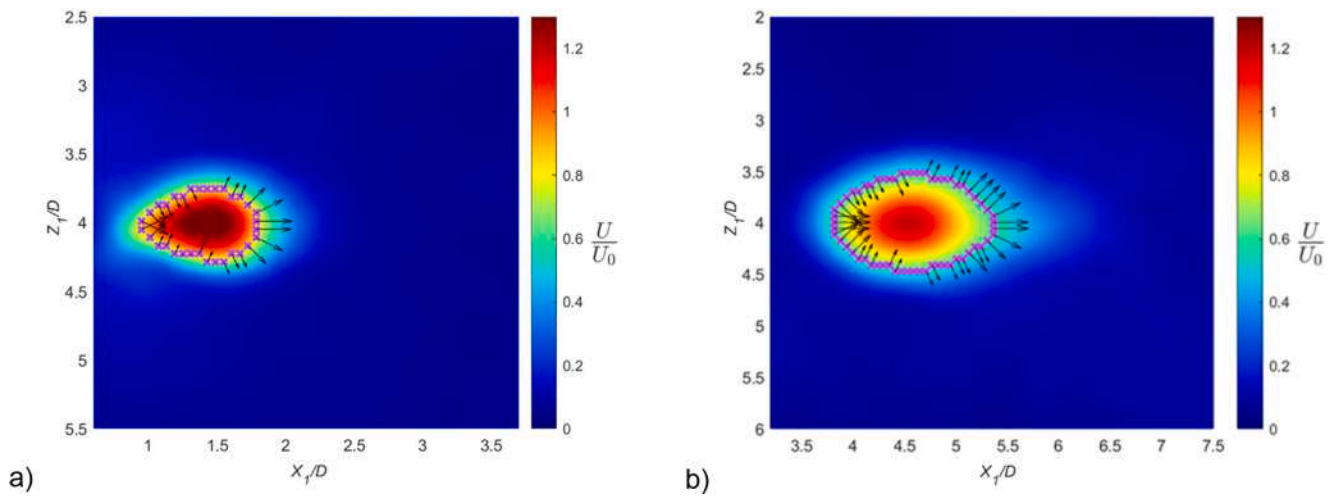

Fig. 17. Circular plunging jets mean velocity magnitude fields in Plane1 for a) $Re_D \approx 11000$ and b) $Re_D \approx 22000$. Purple markers represent the jet boundary as the locus of half of the local maximum velocity value. Black arrows are the jet normally reprojected velocity vectors, properly scaled for visual purpose. (For interpretation of the references to colour in this figure legend, the reader is referred to the web version of this article.)

greater intrinsic instability of the rectangular jet, which triggers a counter-clockwise circulation of the ambient fluid. The 8-shape footprint is found to be more stretched towards the upper region of the jet for higher Reynolds numbers, while in the lower case it is no longer observed even after a small distance below the plunging point. As a matter of fact, as the Reynolds number is decreased, the wideness of the jet vertical sheet (thus the jet footprint main dimension at the plunging point; see Fig. 3a) after the axis switching decreases too, along with velocity and flow rate. Thus, we can infer that the surface tension force acting on the jet before the axis switching meets a weaker inertial force (proportional to the mass flow rate per unit area), so that the footprint area can reach a shape closer to a circular one at the plunging point. Consistently, solidity of footprints (i.e. the ratio between its area and its convex hull area, the latter defined as the smallest convex polygon that contain the footprint) in plane 1 is ≈0.92 for Reynolds number 11000, while it's about ≈0.88 for Reynolds number 20000. Major and minor axis lengths are respectively ≈0.8 x/D and ≈0.6 x/D in the former case, while ≈2.5 x/D and ≈0.6 x/D in the latter. Circular plunging jets show solidity values of about 0.98 for both Reynolds number equal to 11500 and 22000 in plane 1, greater than those of rectangular case. This is confirmed in all tests. Its major and minor axis lengths are respectively ≈1.26 x/D and ≈0.73 x/D for Reynolds number equal to 11500, and ≈1.55 x/D and ≈0.95 x/D for Reynolds number equal to 22000.

In order to estimate flow entrainment, *iso*-velocity lines are computed and velocity vectors are reprojected normally to them. An example of reprojected vectors for the *iso*-line $U/U_0 = 0.5$ is reported in Fig. 17. Following Capone and colleagues [52], entrainment rate is derived from the mass balance of a jet's differential control volume:

$$\frac{\partial Q_a}{\partial x} dx = dQ_r = \oint U \bullet \hat{n} dl dx, \tag{11}$$

$$\frac{d\frac{Q_r}{Q_0}}{d\frac{x}{D}} = \frac{D}{Q_0} \oint U_r(l,x) dl. \tag{12}$$

where Q_a is the flow rate along the jet axial direction x, Q_r the radial flow rate, l is the *iso*-velocity line abscissa, U_r is its orthogonal velocity component (positive for inflow and negative for outflow).

Circular results suggest that local entrainment rate in streamwise direction is increasing with distance from the jet centerline for every Reynolds number (Fig. 19). At a fixed r/D (where r is an equivalent radius derived from each of *iso*-line abscissa, $r = \frac{l}{2\pi}$), higher values are obtained for Reynolds number 11500 and plane 1. Meanwhile, for plane 2, Reynolds number 11500 and Reynolds number equal to 22000 show similar values till about r/D≈0.8, from which the former diverge significantly from the latter.

However, final entrainment rates are almost the same for both the jets, even though for lower Reynolds numbers they are reached at shorter distances r/D due to the earlier rise of the entrainment rate trend itself. This fact can be ascribed to a more intense and faster turbulent production, as already observed in vertical plane measurements (see Fig. 9). Therefore, better mixing performances of low Reynolds number circular jets are confirmed. Moreover, these trends are qualitatively in agreement with Capone and colleagues [52] results, which point out a clear distinction in terms of entrainment rate between the lowest Reynolds number and the highest one. By recalling the velocity' sign statement of eq. (12), we see that a positive entrainment rate involves a positive difference between the inflow and outflow in the measurement plane, so that this flow excess must go outside of it. At the same time, Fig. 12 shows an increasing tendency of the flow rate in the vertical plane, thus we can speculate that the excess from the horizontal plane is moved to the vertical plane, where the shear layers increase their width. Indeed, the entity of the lateral contribution of flow rate in the vertical plane is not enough to justify its increment. This means that for circular plunging jets, ambient flow is mainly entrained due to side inward contribution, then interacts with the jet's boundaries and eventually it's dragged in streamwise direction by the jet main flow.

Rectangular jets exhibit a different behaviour. Entrainment rate from horizontal planes shows a decreasing tendency for all the considered Reynolds numbers, until a negative minimum, from which it starts to grow again (Fig. 19). Positive values are associated to an inflow greater than the outflow, while negative values represent the vice versa. In Plane 1, Reynolds number 11000 has the highest de-entrainment rate value (we say "de-entrainment" owing to the resulting outward motion of fluid from the jet), even though it suddenly grows up to zero at about r/D≈0.65. Meanwhile, Reynolds number 19000 values decrease until about r/D≈0.8, from which it increases, becomes positive and grows in the radial direction. On the other hand, Plane 2 and Reynolds number 11000 shows a decreasing-increasing sequence which goes from a de-entrainment phase to a positive entrainment one. Moreover, this time de-entrainment peak is associated to the highest Reynolds numbers, from which it starts to grow in radial direction too. Owing to the mass conservation law, these results suggest an outward movement of the flow from the vertical plane to the horizontal ones. Indeed, as the jet evolve downstream, flow rate in Fig. 13 decreases, while horizontal plane outflow increases.

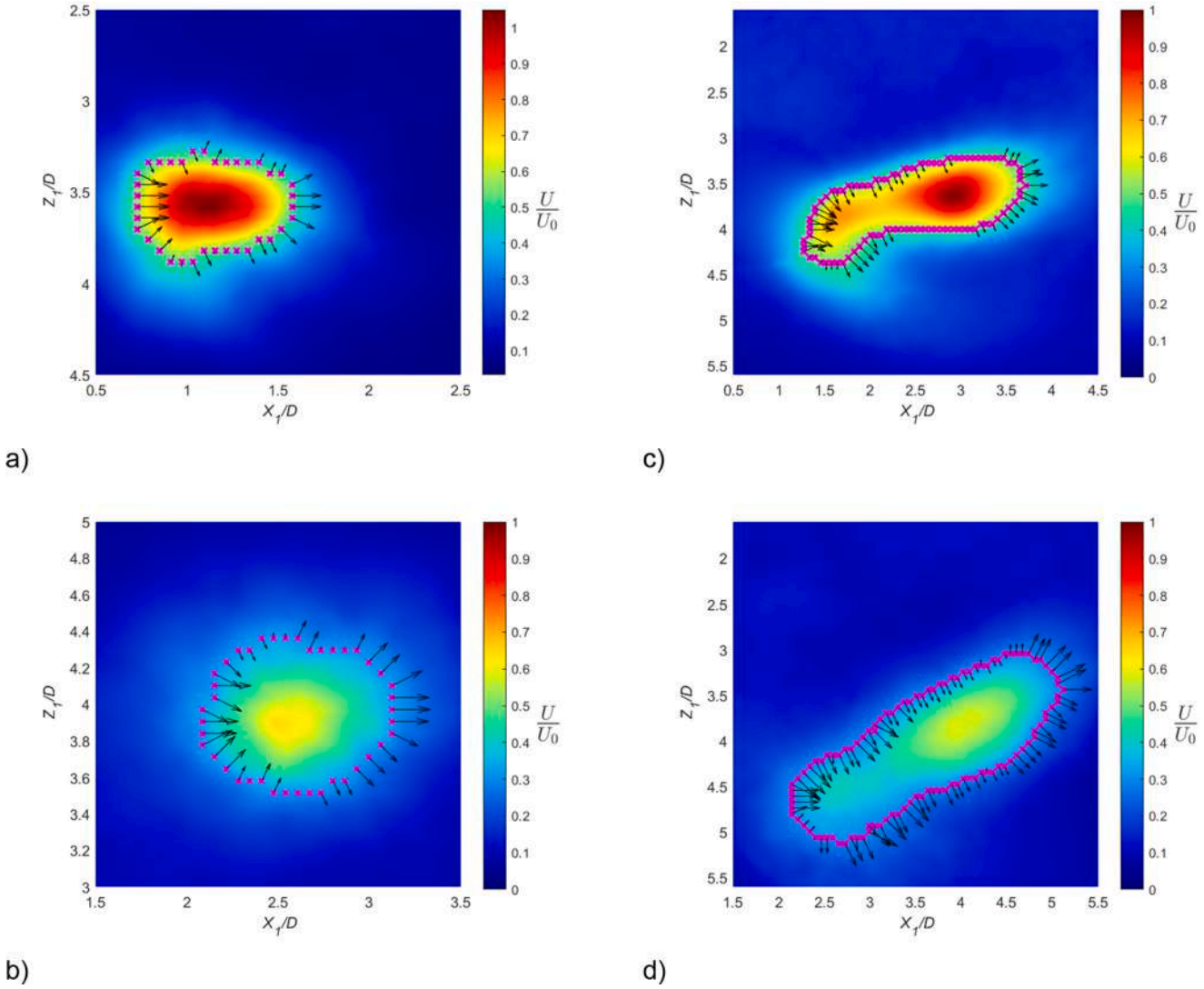

Fig. 18. Rectangular plunging jets mean velocity magnitude fields in Plane 1 for a) Re_D≈11000 and c) Re_D≈19000 and Plane 2 for b) Re_D≈11000 and d) Re_D≈20000. Purple markers represent the jet boundary as the locus of half of the local maximum velocity value. Black arrows are the jet normally reprojected velocity vectors, properly scaled for visual purpose. (For interpretation of the references to colour in this figure legend, the reader is referred to the web version of this article.)

3.5. Time and space integral scales

In order to investigate the presence of dominant coherent structures, cross-correlations of velocity time-signals are computed at different positions along upper and lower jet boundaries, other than jet centerline, in vertical planes (see Fig. 4). Strictly speaking, locations x/D=2, 3, 4, 5 and 6 are chosen as the most suitable for finding well-developed vortices and simultaneously avoiding deviation effects due to the pool floor. The correlation function is defined as:

$$\rho_{uu}(x,y,\tau) = \frac{\overline{u'_{reproj}(x_1,y,t) \bullet u'_{reproj}(x_2,y,t-\tau)}}{\sigma_{x1}\sigma_{x2}} \tag{13}$$

where σ_{x1} and σ_{x2} are the standard deviations of the streamwise velocity time-signals u_{reproj} at positions x_1 and x_2, u'_{reproj} is the velocity fluctuation and τ is the lag time. Positions x_2 is taken downstream of x_1, thus $x_2 > x_1$. Owing to the 9-partitions recording scheme for every Reynolds number test, correlations are evaluated in each partition separately and then averaged to obtain a more robust single-mean correlation signal. Then, correlation peaks are identified, thus obtaining the corresponding lag time and frequency f. In this way, Strouhal numbers are computed as $St = \frac{f \bullet D}{U_0}$. We report in Fig. 20 an example of the averaged correlation between x/D=3 and x/D=4 for circular case at Reynolds number≈25500, along a) jet centerline, b) upper boundary and c) lower boundary. A clear peak is observed in a) at τ ≈-15 ms, while in b) and c) it is localized at ≈–22 ms and ≈–23.5 ms respectively. Results of Strouhal number for circular jets are reported in Table 4, while for rectangular jets they are shown in Table 5. Values along jet centerline are always greater than those of the jet boundaries, but they all exhibit a decreasing tendency in streamwise direction and seems to converge. The former behaviour can be addressed to the interaction between vortices and the ambient fluid. Indeed, they grow in size and reduce their convection velocity as they entrain fluid till a certain distance, where they become unstable and breakup in finer structures [53 4]. On the other hand, convergence can be explained as an effect of the closure of shear layers, thus the faster their growth, the faster is the convergence. Similar trends were observed by Suresh and colleagues [21] for a plane turbulent jet issuing from a rectangular nozzle and Reynolds numbers 250-6250. Moreover, values of upper and lower part of each of our jets are quite similar in almost all test sections, so that one can expect the same vortices size in both the shear layers. Same considerations apply to our rectangular jets, even though for Reynolds number equal to 19000 and

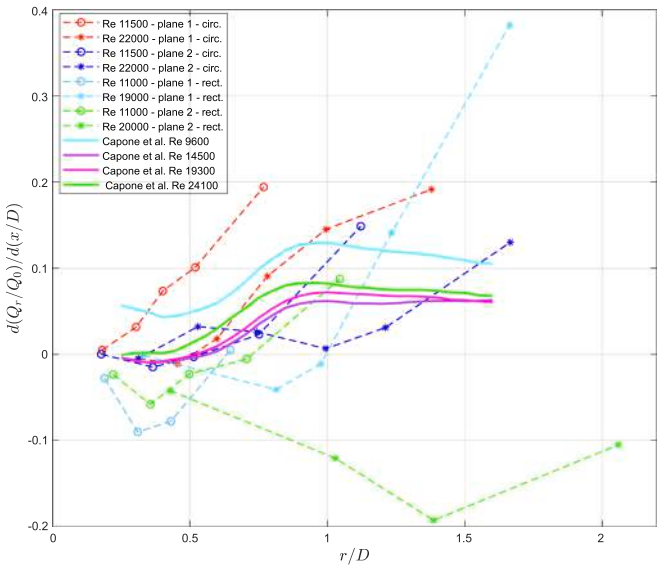

Fig. 19. Entrainment rate evaluated at two horizontal planes: plane 1 it is at about 7 cm (Y/D≈3.5) above the pool floor, plane 2 it is at about 4 cm (Y/D≈2.25) above the pool floor. Literature results are obtained for free circular jets at about x/D=0.75.

25000, Strouhal numbers between x/D =2–3 and x/D =3–4 are not reported because correlation was not observed there. Probably, this fact can be ascribed to the rotation of the jets around their axis.

In Fig. 21 we report an example of vortex passage for a circular jet at Reynolds number≈25500, along its upper boundary, between jet cross sections x/D=2.5 and x/D=3.5.

The relation between frequency and Reynolds number is also investigated. Speaking about circular jets, frequency seems to increase with Reynolds number, so that Re_D≈18000 and ≈25500 jets have closer values at each streamwise location than Re_D≈11000. As an example, f ≈34 Hz between x/D =4–5 along centerline for Re_D≈11000 case, while it is about 62.5 Hz for Re_D≈25500. These results are consistent with the well-known Strouhal number independency on Reynolds number (for Re_D>2000, as reported by Suresh and colleagues [21]).

Rectangular jets exhibit similar behaviours, even though this time differences in frequency are smaller among all tests. Thus, Strouhal numbers seems to slightly decrease when increasing Reynolds numbers along the centerline. For example, St≈1.741 for the lowest Reynolds number case and ≈0.979 for the highest one. However, values in the upper and lower side look quite in agreement in all jets. Therefore, one might conclude that vortices evolution in streamwise direction is similar for both circular and rectangular jets.

Our results are quite in agreement to Mi and colleagues [17], who reported a value of Strouhal number of about 0.7 at x/D=3 for a turbulent air jet from an orifice plate at Re_D≈16000 in the shear layers. A close value was obtained also by Violato and Scarano [54], who investigated circular and 6-chevron jets at Reynolds number equal to 5000. In the former case, they saw the shedding of axisymmetric vortices at St=0.72, while in the latter a pulsatile motion in range St=0.56–0.85 was observed in the potential core. Meanwhile Namer and Ötügen [20] found an approximately constant value of ≈0.273 at x/D=5 and y/D=0.5 for plane air jets at Re_D=1000–7000. They stated that Strouhal number independency on Reynolds number leads to an independency also of vortices formation per unit length. Therefore, differences in mixing rate among jets number are connected to the relative strength of large vortices and not to their size. On the other hand, Becker and Massaro [55] found a clear dependence on Reynolds number for pure tone excited air jets issuing from a nozzle in Reynolds number range

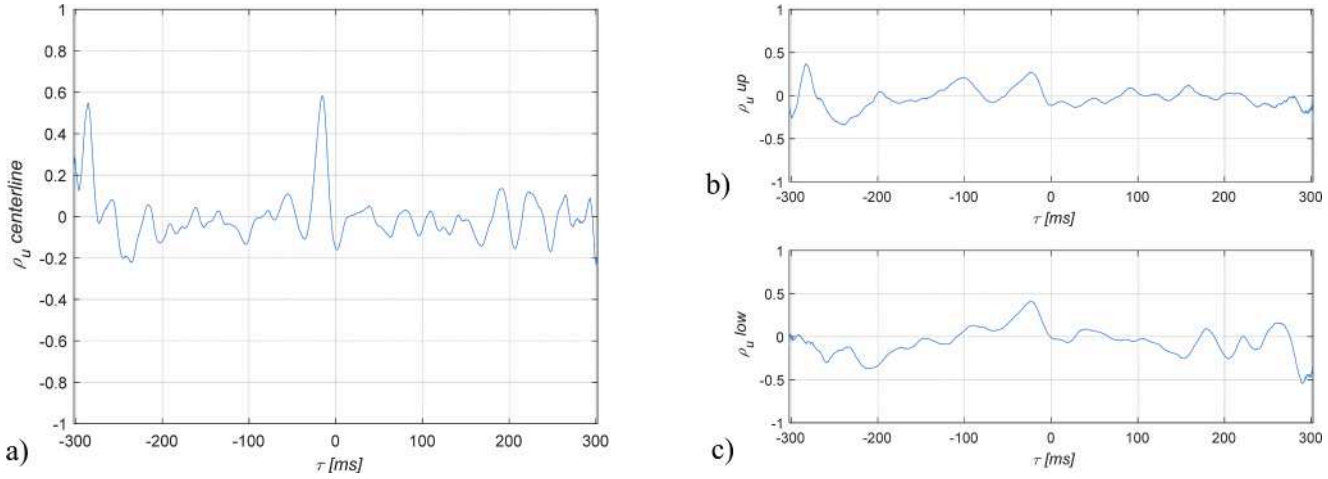

Fig. 20. Cross-correlation function between positions at x/D=3 and x/D=4 for a circular plunging jet at Reynolds number≈25500 along a) jet centerline b) upper boundary c) lower boundary.

Table 4

Main Strouhal numbers ($St = \frac{f \bullet D}{U_0}$) for circular plunging jets as derived from cross-correlations between streamwise locations x/D =2, 3, 4, 5 and 6 along the jets' centerline and boundaries (i.e. half-velocity width positions). Aiming to avoid pool floor effects, results for cross-correlation between x/D=5 and 6 are not reported at Re_D≈11000.

	Re_D 11000			Re_D 18000			Re_D 25500		
Sez. x/D	St_{up}	St_{low}	$St_{centerline}$	St_{up}	St_{low}	$St_{centerline}$	St_{up}	St_{low}	$St_{centerline}$
2–3	1.424	0.848	1.572	0.955	1.061	1.447	0.907	0.780	1.290
3–4	1.161	1.006	1.301	0.838	0.735	1.137	0.762	0.714	1.118
4–5	0.920	0.888	1.279	0.525	0.868	0.955	0.860	0.714	1.048
5–6	–	–	–	0.531	0.604	0.783	0.550	0.541	0.818

Table 5

Main Strouhal numbers ($St = \frac{f \bullet D}{U_0}$) for rectangular plunging jets as derived from cross-correlations between streamwise locations x/D = 2, 3, 4 and 5 along the jets' centerline and boundaries (i.e. half-velocity width positions). Results between x/D = 2–3 at $Re_D \approx 19000$ and ≈ 25000 are not reported here because no correlation was observed in these cases.

	Re_D 13000			Re_D 15000			Re_D 19000			Re_D 25000		
Sez. x/D	St_{up}	St_{low}	$St_{centerline}$	St_{up}	St_{low}	$St_{centerline}$	St_{up}	St_{low}	$St_{centerline}$	St_{up}	St_{low}	$St_{centerline}$
2–3	0.984	1.014	1.787	0.809	0.722	1.619	1.005	–	1.560	0.903	–	1.468
3–4	0.943	1.151	1.741	0.742	0.712	1.444	0.718	0.794	1.371	0.665	0.607	1.036
4–5	0.918	0.930	1.656	0.694	0.621	1.187	0.686	0.656	1.028	0.705	0.550	0.979

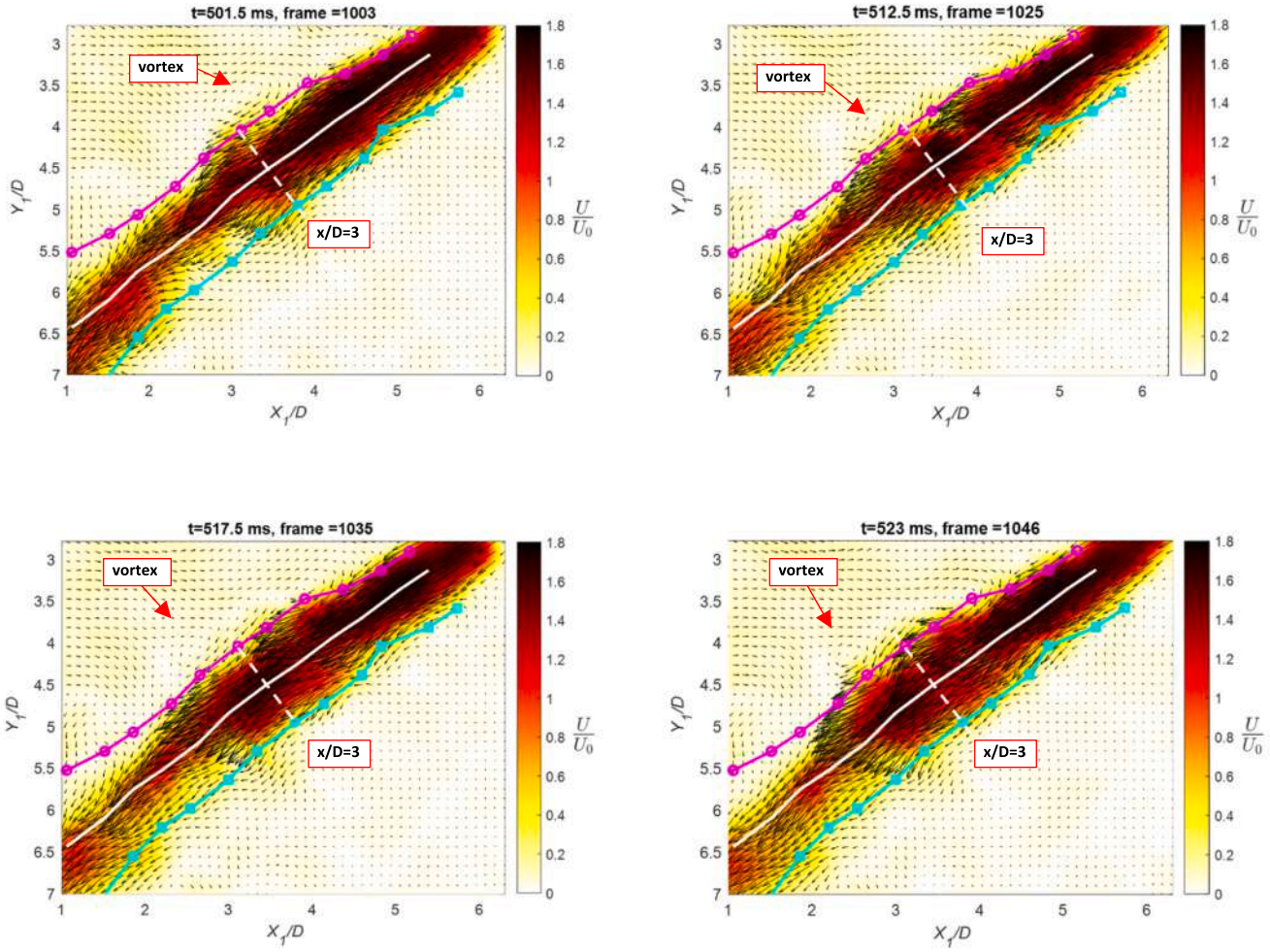

Fig. 21. Instantaneous velocity fields of a circular jet at Re_D=25500 in a time interval of 21.5 ms, between frame 1003 to frame 1046. Please, note the vortex progression along the upper boundary, from (a) to (d): (a) vortex at x/D≈2.5, (b) vortex at about x/D≈3. Topological loci are reported with lines of different colours: magenta and cyan lines indicate jet upper and lower limit respectively (as derived from the half-velocity width), while white line is the jet axis (as derived from the loci of the maximum velocity. Markers on each line lay on uniform-spaced jet cross sections with a step of 0.5D. (For interpretation of the references to colour in this figure legend, the reader is referred to the web version of this article.)

1000–15000, so that $St = 0.012\sqrt{Re}$. Nevertheless, they observed also a similar Strouhal numbers distribution even for unexcited jets. In light of these findings, one should remind that vortices are originated by the roll-up of the shear layers due to amplification of disturbances in Kelvin-Helmholtz instability. Perturbations are strictly related to the facility of the experiment [5620] and vary with Reynolds numbers. Therefore, some differences in Strouhal numbers can be explained in this way.

4. Conclusion

We studied the behaviour of water jets issuing horizontally in air from circular and rectangular orifices and then plunging in a pool. Reynolds numbers based on the orifice diameter were between ≈11000 and ≈25000. Topological aspects were investigated before and after the impact with the free surface, while velocity fields, entrainment rate and rms profiles were evaluated only below the plunging point. Measurements were performed in a vertical middle plane and in two horizontal planes. Rectangular jets showed axis switching before impacting on the free surface. They were characterized by an asymmetrical shape of their cross profiles, which was preserved even at some diameters far away in streamwise direction, before reaching an axisymmetrical shape (when reached). As Reynolds number was decreased, axisymmetry was found

to rise earlier. Meanwhile, by increasing the Reynolds number, a double jet-like appearance was observed along with an "8" shape footprint at the plunging point. However, asymmetry was found also in circular jets, with a different dependence on the Reynolds number. This time, as Reynolds number was decreased, asymmetry became predominant along most of the jets' evolution. Both rectangular and circular jets pointed out a spreading behaviour in streamwise direction below the free surface. Circular jets confirmed the results obtained by Hassan and colleagues [4] for vertical round plunging jets which showed a higher mixing ability than free round jets. However, our results revealed an even better mixing than of those vertical jets. The lowest circular Reynolds number jet was characterized by the highest centerline velocity decays, spreading of the cross-sections, rms profiles and ambient mass entrainment rate than the other circular jets. Meanwhile, for rectangular jets, the same results were obtained in the highest Reynolds number case. Jet plunging angle was found to play a role in our experiment. Indeed, high values were associated to the presence of an intense co-flow in the lower side of jets, while lower ones revealed the rise of another intense co-flow in the upper part. Therefore, in circular jets, as Reynolds number was increased, flow rate and half-velocity width behaviours became similar in both the upper and lower side of jets, thus confirming the vanishing of asymmetry. Meanwhile, even if similar considerations can be done for the upper part of rectangular jets, the lower one showed a different evolution. This is due to the early vanishing of the lower round jet observed in the double jet-like configuration of high Reynolds numbers.

Horizontal and vertical planes entrainment rate pointed out the different distribution of the flow between them for circular and rectangular jets. Indeed, the former revealed a flow moving from horizontal to vertical planes, while the latter showed an opposite behaviour, thus from vertical to horizontal ones. Therefore, circular jets involved ambient fluid to increase their width in streamwise direction, acting like a sink, while rectangular jets behaved more like a source of flow for the rest of the pool.

Finally, main vortices evolution was studied along jet centerline and at the half-velocity width positions (both in the upper and lower side). Strouhal numbers were computed and found to have a decreasing trend in streamwise direction. A convergence tendency was observed among centerline, upper and lower side for all jets, which is associated to the grow of shear layers. On the other hand, no significant differences were derived at the same streamwise location for all jets, even when changing orifice's geometry. Therefore, Strouhal number independency on Reynolds number is observed in our tests.

The present work involved only two geometries which were considered as representative of a clear symmetrical and non-symmetrical situation. However, further investigations are needed to improve the understanding of plunging jets behaviour varying orifice geometries. Three-dimensional effects can be further detailed by focusing on smaller region of jets, using stereoscopic or tomographic PIV. Moreover, velocity range was limited due to avoiding most of air bubbles entrainment, but in order to have a general description of these jets they will be considered in future works.

CRediT authorship contribution statement

Giorgio Moscato: Data curation, Visualization, Methodology. **Giovanni Paolo Romano:** Methodology, Conceptualization.

Declaration of Competing Interest

The authors declare that they have no known competing financial interests or personal relationships that could have appeared to influence the work reported in this paper.

Data availability

Data will be made available on request.

Acknowledgment

This work has been supported by the PRIN project on Advanced Computations and Experiments on Multiphase Flows – 2019, funded by the MUR (Italian Office for Research). The authors would like to thank Dr. Alessandro Capone for his help during the analysis of the data, along with Maximo Capponi, Alessandro Caterina and Dr. Antonello Binni for their precious help and suggestions in implementing and optimizing the experimental setup.

Declarations

Funding: this work was funded by MUR (Italian Office for Research) in the framework of a PRIN project on Advanced Computations and Experiments on Multiphase Flows - 2019.

Conflicts of interest/Competing interests: the authors report no conflict of interest.

Availability of data and material: data and material are available on request to the corresponding author.

Code availability: not applicable.

References

[1] T. Bagatur, N. Sekerdag, Air-entrainment characteristics in a plunging water jet system using rectangular nozzles with rounded ends, Water SA 29 (2003) 35–38, https://doi.org/10.4314/wsa.v29i1.4943.
[2] J.A. Moulijn, Chemical Process Technology (2013), https://doi.org/10.5860/choice.51-2107.
[3] M. El Hammoumi, J.L. Achard, L. Davoust, Measurements of air entrainment by vertical plunging liquid jets, Exp. Fluids 32 (2002) 624–638, https://doi.org/10.1007/s00348-001-0388-1.
[4] S.H. Hassan, T. Guo, P.P. Vlachos, Flow field evolution and entrainment in a free surface plunging jet, Phys. Rev. Fluids 4 (2019) 1–17, https://doi.org/10.1103/PhysRevFluids.4.104603.
[5] A.K. Bińi, Gas entrainment by plunging liquid jets, Chem. Eng. Sci. 48 (1993) 3585–3630, https://doi.org/10.1016/0009-2509(93)81019-R.
[6] K.J. Sene, Air entrainment by plunging jets, Chem. Eng. Sci. 43 (1988) 2615–2623, https://doi.org/10.1016/0009-2509(88)80005-8.
[7] K.J. Hammad, Liquid jet impingement on a free liquid surface: PIV study of the turbulent bubbly two-phase flow, (2010) 1–9. https://doi.org/10.1115/FEDSM-ICNMM2010-31248.
[8] K.T. Kiger, J.H. Duncan, Air-entrainment mechanisms in plunging jets and breaking waves, Annu. Rev. Fluid Mech. 44 (2011) 563–596, https://doi.org/10.1146/annurev-fluid-122109-160724.
[9] I. Shrivastava, E.E. Adams, B. Al-Anzi, A.C. Chow, J. Han, Confined plunging liquid jets for dilution of brine from desalination plants, Processes. 9 (2021) 856, https://doi.org/10.3390/pr9050856.
[10] E.J. Gutmark, F.F. Grinstein, Flow control with noncircular jets, Annu. Rev. Fluid Mech. 31 (1999) 239–272, https://doi.org/10.1146/annurev.fluid.31.1.239.
[11] S.S. Aleyasin, M.F. Tachie, M. Koupriyanov, Statistical properties of round, square, and elliptic jets at low and moderate Reynolds numbers, J. Fluids Eng. Trans. ASME. 139 (2017) 1–11, https://doi.org/10.1115/1.4036824.
[12] M. Azad, W.R. Quinn, D. Groulx, Mixing in turbulent free jets issuing from isosceles triangular orifices with different apex angles, Exp. Therm Fluid Sci. 39 (2012) 237–251, https://doi.org/10.1016/j.expthermflusci.2012.01.028.
[13] S.S. Aleyasin, M.F. Tachie, M. Koupriyanov, PIV measurements in the near and intermediate field regions of jets issuing from eight different nozzle geometries, flow, Turbul. Combust. 99 (2017) 329–351, https://doi.org/10.1007/s10494-017-9820-3.
[14] K.B.M.Q. Zaman, Axis switching and spreading of an asymmetric jet - role of vorticity dynamics, 33rd Aerosp Sci. Meet. Exhib. 316 (1995) 1–27, https://doi.org/10.2514/6.1995-889.
[15] M. Tadjfar, A. Jaberi, Effects of aspect ratio on the flow development of rectangular liquid jets issued into stagnant air, Int. J. Multiph. Flow 115 (2019) 144–157, https://doi.org/10.1016/j.ijmultiphaseflow.2019.03.011.
[16] S.G. Taylor, Formation of thin flat sheets of water, Proc. R. Soc. (1961). https://doi.org/https://doi.org/10.1098/rspa.1960.0207.
[17] J. Mi, G.J. Nathan, D.S. Nobes, Mixing characteristics of axisymmetric free jets from a contoured nozzle, an orifice plate and a pipe, J. Fluids Eng. Trans. ASME. 123 (2001) 878–883, https://doi.org/10.1115/1.1412460.
[18] J. Mi, P. Kalt, G.J. Nathan, C.Y. Wong, PIV measurements of a turbulent jet issuing from round sharp-edged plate, Exp. Fluids 42 (2007) 625–637, https://doi.org/10.1007/s00348-007-0271-9.

[19] W.R. Quinn, Upstream nozzle shaping effects on near field flow in round turbulent free jets, Eur. J. Mech. B/Fluids. 25 (2006) 279–301, https://doi.org/10.1016/j.euromechflu.2005.10.002.
[20] I. Namer, M.V. Ötügen, Velocity measurements in a plane turbulent air jet at moderate Reynolds numbers, Exp. Fluids 6 (1988) 387–399, https://doi.org/10.1007/BF00196484.
[21] P.R. Suresh, K. Srinivasan, T. Sundararajan, S.K. Das, Reynolds number dependence of plane jet development in the transitional regime, Phys. Fluids 20 (2008), https://doi.org/10.1063/1.2904994.
[22] J. Mi, M. Xu, T. Zhou, Reynolds number influence on statistical behaviors of turbulence in a circular free jet, Phys. Fluids 25 (2013), https://doi.org/10.1063/1.4811403.
[23] A. Capone, A. Soldati, G.P. Romano, Mixing and entrainment in the near field of turbulent round jets, Exp. Fluids 54 (2013), https://doi.org/10.1007/s00348-012-1434-x.
[24] A. Hashiehbaf, G.P. Romano, Particle image velocimetry investigation on mixing enhancement of non-circular sharp edge nozzles, Int. J. Heat Fluid Flow 44 (2013) 208–221, https://doi.org/10.1016/j.ijheatfluidflow.2013.05.017.
[25] E. van de Sande, J.M. Smith, Mass transfer from plunging water jets, Chem. Eng. J. 10 (1975) 225–233, https://doi.org/10.1016/0300-9467(75)88040-3.
[26] E. Van De Sande, J.M. Smith, Jet break-up and air entrainment by low velocity turbulent water jets, Chem. Eng. Sci. 31 (1976) 219–224, https://doi.org/10.1016/0009-2509(76)85060-9.
[27] T. Bagatur, F. Onen, Prediction of flow and oxygen transfer by a plunging water jets with genetic expression programming (GEP) models, Arab. J. Sci. Eng. 39 (2014) 4421–4432, https://doi.org/10.1007/s13369-014-1092-9.
[28] N. Bertola, H. Wang, H. Chanson, A physical study of air–water flow in planar plunging water jet with large inflow distance, Int. J. Multiph. Flow 100 (2018) 155–171, https://doi.org/10.1016/j.ijmultiphaseflow.2017.12.015.
[29] K. Harby, S. Chiva, J.L. Muñoz-Cobo, An experimental study on bubble entrainment and flow characteristics of vertical plunging water jets, Exp. Therm Fluid Sci. 57 (2014) 207–220, https://doi.org/10.1016/j.expthermflusci.2014.04.004.
[30] H. Chanson, P.D. Cummings, An experimental study on air carryunder due to a plunging liquid jet, Int. J. Multiph. Flow 20 (1994) 667–670, https://doi.org/10.1016/0301-9322(94)90037-X.
[31] H. Chanson, T. Brattberg, Air entrainment by two-dimensional plunging jets: The impingement region and the very-near flow field, Am. Soc. Mech. Eng. Fluids Eng. Div. FED. (1998) 1–8.
[32] F. Di Nunno, F.A. Pereira, M. Miozzi, F. Granata, R. Gargano, G. De Marinis, F. Di Felice, Experimental study of a vertical plunging jet by means of a volumetric shadowgraph technique, J. Phys. Conf. Ser. 1589 (2020), https://doi.org/10.1088/1742-6596/1589/1/012006.
[33] X. Qu, A. Goharzadeh, L. Khezzar, A. Molki, Experimental characterization of air-entrainment in a plunging jet, Exp. Therm Fluid Sci. 44 (2013) 51–61, https://doi.org/10.1016/j.expthermflusci.2012.05.013.
[34] Y. Ma, L. Zhang, Y. Yang, P. Wei, Air entrainment by inclined circular plunging water jets with various impingement heights, Water Sci. Technol Water Supply 20 (2020) 3478–3486, https://doi.org/10.2166/ws.2020.246.
[35] M.S. Baawain, M. Gamal El-Din, D.W. Smith, Characterizing two inclined circular water jets plunging into an aeration tank, Int. J. Multiph. Flow 40 (2012) 158–165, https://doi.org/10.1016/j.ijmultiphaseflow.2011.10.012.
[36] D. Vouk, G. Gjetvaj, D. Malus, Wastewater aeration using plunging water jet aerators, Int. Symp. Water Manag. Hydraul. Eng. (2005) 313–322.
[37] F. Granata, G. de Marinis, R. Gargano, W.H. Hager, Hydraulics of circular drop manholes, J. Irrig. Drain. Eng. 137 (2011) 102–111, https://doi.org/10.1061/(asce)ir.1943-4774.0000279.
[38] A. Hashiehbaf, G.P. Romano, A phase averaged PIV study of circular and non-circular synthetic turbulent jets issuing from sharp edge orifices, Int. J. Heat Fluid Flow 82 (2020), 108536, https://doi.org/10.1016/j.ijheatfluidflow.2020.108536.
[39] M. Raffel, C.E. Willert, F. Scarano, C.J. Kähler, S.T. Wereley, J. Kompenhans, Particle Image Velocimetry (2018), https://doi.org/10.1007/978-3-319-68852-7.
[40] M. Falchi, G.P. Romano, Evaluation of the performance of high-speed PIV compared to standard PIV in a turbulent jet, Exp. Fluids 47 (2009) 509–526, https://doi.org/10.1007/s00348-009-0682-x.
[41] W. Thielicke, E.J. Stamhuis, PIVlab – towards user-friendly, affordable and accurate digital particle image velocimetry in MATLAB, J. Open Res. Softw. 2 (2014), https://doi.org/10.5334/JORS.BL.
[42] J. Mi, G.J. Nathan, Statistical properties of turbulent free jets issuing from nine differently-shaped nozzles, Flow Turbul. Combust. 84 (2010) 583–606, https://doi.org/10.1007/s10494-009-9240-0.
[43] J.M. Carrillo, F. Marco, L.G. Castillo, J.T. García, Experimental study of submerged hydraulic jumps generated downstream of rectangular plunging jets, Int. J. Multiph. Flow 137 (2021), https://doi.org/10.1016/j.ijmultiphaseflow.2021.103579.
[44] L. Rayleigh, Proc. Roy. Soc. London Ser. A 29 (1879) 71–97.
[45] S.E. Bechtel, The oscillation of slender elliptical inviscid and newtonian jets: Effects of surface tension, inertia, viscosity, and gravity, J. Appl. Mech. Trans. ASME. 56 (1989) 968–974, https://doi.org/10.1115/1.3176198.
[46] S.S. Aleyasin, N. Fathi, M.F. Tachie, P. Vorobieff, M. Koupriyanov, On the development of incompressible round and equilateral triangular jets due to reynolds number variation, J. Fluids Eng. Trans. ASME. 140 (2018) 1–12, https://doi.org/10.1115/1.4040031.
[47] A. Krothapalli, D. Baganoff, K. Karamcheti, On the mixing of a rectangular jet, J. Fluid Mech. 107 (1981) 201–220, https://doi.org/10.1017/S0022112081001730.
[48] W.R. Quinn, Turbulent free jet flows issuing from sharp-edged rectangular slots: The influence of slot aspect ratio, Exp. Therm Fluid Sci. 5 (1992) 203–215, https://doi.org/10.1016/0894-1777(92)90007-R.
[49] H. Tennekes, J.L. Lumley, Spectral Dynamics, in: A First Course Turbul, The MIT Press, 1972. https://doi.org/10.7551/mitpress/3014.003.0010.
[50] F.P. Ricou, D.B. Spalding, Measurements of entrainment by axisymmetrical turbulent jets, J. Fluid Mech. 11 (1961) 21–32, https://doi.org/10.1017/S0022112061000834.
[51] D. Han, M.G. Mungal, Direct measurement of entrainment in reacting/nonreacting turbulent jets, Combust. Flame 124 (2001) 370–386, https://doi.org/10.1016/S0010-2180(00)00211-X.
[52] A. Capone, A. Soldati, G.P. Romano, Mixing and entrainment in the near field of turbulent round jets, Exp. Fluids 54 (2013) 1–22, https://doi.org/10.1007/s00348-012-1434-x.
[53] V.W. Goldschmidt, M.F. Young, E.S. Ott, Turbulent convective velocities (broadband and wavenumber dependent) in a plane jet, J. Fluid Mech. 105 (1981) 327–345, https://doi.org/10.1017/S0022112081003236.
[54] D. Violato, F. Scarano, Three-dimensional evolution of flow structures in transitional circular and chevron jets, Phys. Fluids 23 (2011), https://doi.org/10.1063/1.3665141.
[55] H.A. Becker, T.A. Massaro, Vortex evolution in a round jet, J. Fluid Mech. 31 (1968) 435–448, https://doi.org/10.1017/S0022112068000248.
[56] E. Gutmark, C.M. Ho, Preferred modes and the spreading rates of jets, Phys. Fluids 26 (1983) 2932–2938, https://doi.org/10.1063/1.864058.